nature climate change

Article

https://doi.org/10.1038/s41558-025-02397-9

Shifting hotspot of tropical cyclone clusters in a warming climate

Received: 27 September 2024

Accepted: 3 July 2025

Published online: 31 July 2025

Check for updates

Zheng-Hang Fu[1,2,10], Dazhi Xi[3,4,10], Shang-Ping Xie[5], Wen Zhou[1,2] ✉, Ning Lin[4], Jiuwei Zhao[6], Xin Wang[1] & Johnny C. L. Chan[7,8,9]

Multiple tropical cyclones can be present concurrently within one ocean basin, and these clusters can induce compound hazards within a short time window. While the western North Pacific has historically been home to most tropical cyclone clusters, how climate change might affect this is unclear. Here we use observations and high-resolution climate model simulations to develop a probabilistic model, assuming that tropical cyclones are mutually independent and occur randomly. Against this baseline, we identify outliers as clusters with dynamic interactions between tropical cyclones. We find that the recent global warming pattern induces major shifts in tropical cyclone cluster hotspots from the western North Pacific to the North Atlantic by modulating tropical cyclone frequency and synoptic-scale wave activity. Our probabilistic modelling indicates a tenfold increase in the likelihood of tropical cyclone cluster frequency in the North Atlantic, surpassing that in the western North Pacific, from 1.4 ± 0.4% to 14.3 ± 1.2% over the past 46 years.

On 14 September 2020, an extreme tropical cyclone (TC) cluster made headlines, with five TCs entrenched over the North Atlantic (NA)[1] (Fig. 1a and Supplementary Fig. 1). That year witnessed an unusually active Atlantic hurricane season, with nine storms forming in succession within 3 weeks (Fig. 1a). Such back-to-back TCs over the NA and their threat to the coastal USA have increased in recent decades[2–4]. Here, we define TC clusters as two or more TCs present simultaneously within the same basin[5,6]. Historically, only 40% of TCs appeared alone, with the majority of TCs coming in clusters[6]. Beyond the combined impacts of individual TCs, TC clusters can lead to disproportionate damage along coastal regions because infrastructure, communities and restoration resources cannot bounce back from the damage from the preceding TC within a short period of time[2,7–9]. In addition, dispatching limited emergency supplies to affected areas is rather difficult when multiple TCs impact different regions concurrently, as exemplified by the Federal Emergency Management Agency's failure to provide adequate support to Hurricane Maria's victims in Puerto Rico after its overextended responses to hurricanes Harvey and Irma in 2017[10].

Although the extreme TC cluster in 2020 is relatively new to Atlantic coastlines, East and Southeast Asian coastal regions have long suffered from such temporally compound events. In late summer 2004, over the western North Pacific (WNP), nine disturbances intensified into TCs within 34 days (refs. 11,12), five of which made landfall in East Asia (Fig. 1b). While the majority of TC clusters historically occur in the WNP, how climate change might affect this preference remains unclear.

Previous studies have analysed large-scale dynamic and thermodynamic conditions that are favourable for TC genesis to investigate

[1]Key Laboratory of Polar Atmosphere-Ocean-Ice System for Weather and Climate, Ministry of Education, Department of Atmospheric and Oceanic Sciences and Institute of Atmospheric Sciences, Fudan University, Shanghai, China. [2]Key Laboratory for Polar Science MNR, Polar Research Institute of China, Shanghai, China. [3]Department of Earth and Planetary Sciences, The University of Hong Kong, Hong Kong, China. [4]Department of Civil and Environmental Engineering, Princeton University, Princeton, NJ, USA. [5]Scripps Institution of Oceanography, University of California San Diego, La Jolla, CA, USA. [6]State Key Laboratory of Climate System Prediction and Risk Management, Institute of Climate and Application Research, Nanjing University of Information Science and Technology, Nanjing, China. [7]Shanghai Typhoon Institute of China Meteorological Administration, Shanghai, China. [8]Asia-Pacific Typhoon Collaborative Research Center, Shanghai, China. [9]School of Energy and Environment, City University of Hong Kong, Hong Kong, China. [10]These authors contributed equally: Zheng-Hang Fu, Dazhi Xi. ✉e-mail: wen_zhou@fudan.edu.cn

https://doi.org/10.1038/s41558-025-02397-9

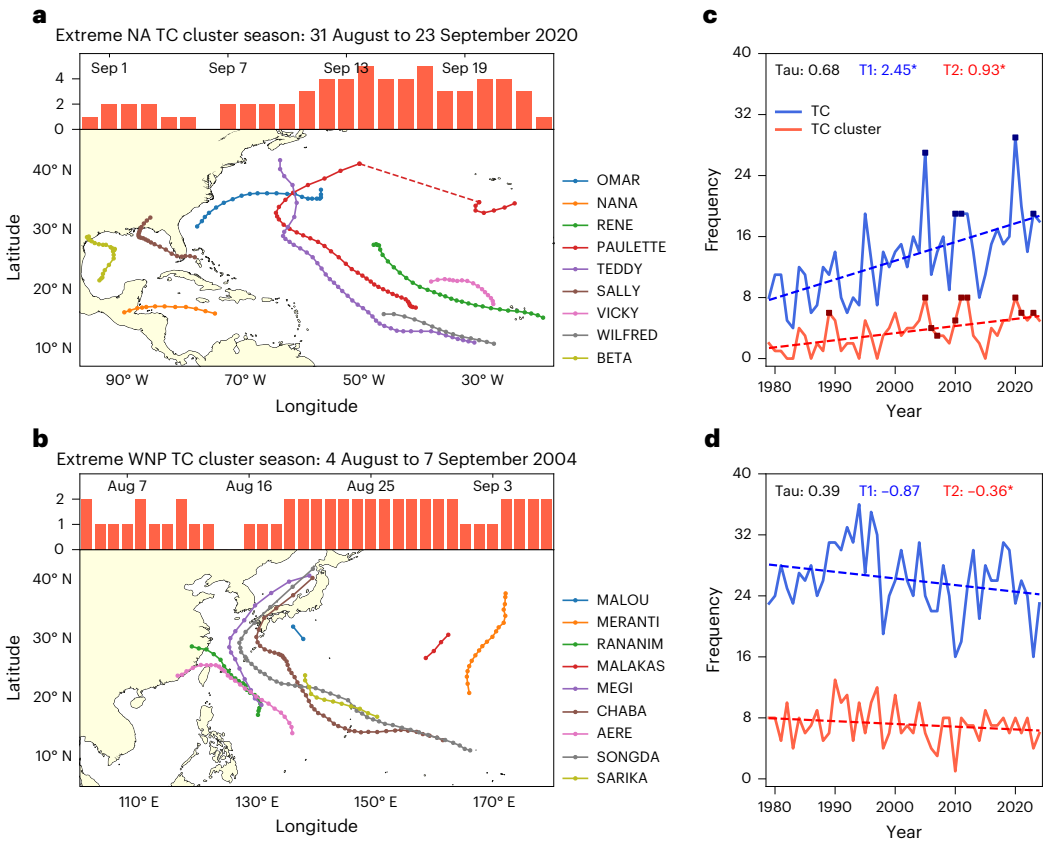

Fig. 1 | Extreme TC cluster seasons and observed changes in TC frequency and TC cluster frequency. a,**b**, The TC activity from 31 August to 23 September 2020 in the NA (**a**) and from 4 August to 7 September 2004 in the WNP (**b**). The histogram shows the daily TC counts within the period, and the map shows coloured tracks for each TC. Hurricane Paulette (red line in **a**) regenerated into a TC after its extratropical transition, so we connect the two tracks with a dotted line. **c**,**d**, Time series of TC frequency (blue lines) and TC cluster frequency (orange lines) during 1979–2024 over the NA (**c**) and WNP (**d**). Kendall rank correlations (Tau) between TC frequency and TC cluster frequency are shown at the top left. The linear trends of TC frequency (T1) and TC cluster frequency (T2) are plotted as dotted lines, with the associated 10-year trend values presented in the top panel. Asterisks denote significance at the 95% confidence level on the basis of the 1,000-sample bootstrapping. Bold dots in **b** indicate that the frequency over the NA reaches or exceeds that over the WNP, occurring in 5 years for TC frequency and 10 years for TC cluster frequency during 1979–2024.

TC cluster formation (for example, refs. 4–6,13). Additionally, recent studies have highlighted changes in TC climatology features, including frequency[14,15], seasonality[16–18] and duration[19,20] under anthropogenic warming. However, understanding how these TC climatology features besides the mechanisms at TC genesis influence TC cluster activity remains a challenge.

Two possible conditions for TC cluster formation exist. First, TC genesis may involve physical processes related to pre-existing TC(s), thus contributing to TC cluster formation[21,22]. TC-induced Rossby wave dispersion[4,5,23,24], synoptic-scale wave trains[12,25,26] and other equatorial waves[21,27,28] can lead to TC cluster formation, when subsequent TCs are pre-conditioned by synoptic-scale cyclonic disturbances (hereafter, 'dynamically connected events'). Second, the TCs in a TC cluster may be independently generated and happen to coincide. Several studies, some mutually conflicting, have tried to delineate the two types of TC cluster formation on the basis of linear wave theory[23,24] or through case studies aided by numerical simulations[29,30]. However, the relative importance of the two mechanisms for TC cluster formation remains unknown owing to the lack of a robust theoretical framework and reliable diagnostic tools.

The present study develops a probabilistic model to establish a baseline of independent random TC occurrence and then identify dynamically connected TC clusters as outliers from the baseline. This method enables us to attribute TC cluster trends to the recent La Niña-like global warming pattern.

TC cluster climatology explained by a probabilistic model

Although the WNP has long been home to most TCs globally, recent decades have witnessed decreasing trends in both TC and TC cluster frequencies in the WNP, accompanied by significant increasing trends in the NA (Fig. 1c,d). Meanwhile, the TC cluster frequency in the NA has reached or even surpassed that of the WNP nine times since 2005 (red dots in Fig. 1c). This indicates that the NA is emerging as a hotspot for TC clusters in recent decades.

The TC cluster frequency is not a linear function of TC frequency, as confirmed by the low Kendall rank correlation in Fig. 1d. Linking the contrasting trends in TC cluster frequency between the two basins to the TC frequency trend is thus not straightforward. Therefore, we develop a probabilistic framework for stochastic TC cluster simulations with TC parameters estimated from observations during 1979–2024 (Fig. 2 and Methods). Probability density functions (PDFs) of TC genesis time are shown in Fig. 2a,b. The window of TC genesis over the NA is confined mainly to August–October, with a yearly peak in September, whereas the window is much wider for the WNP (Fig. 2a,b). Considering the relationship between TC occurrence time and lifespan, we then bin the genesis time into deciles and obtain the corresponding conditional PDF for TC lifespan for each decile of genesis time (Fig. 2c,d), which shows that NA TCs tend to last longer in the TC peak season, and thus TC clusters over the NA tend to be concentrated owing to the overlap of many long-lived TCs.

https://doi.org/10.1038/s41558-025-02397-9

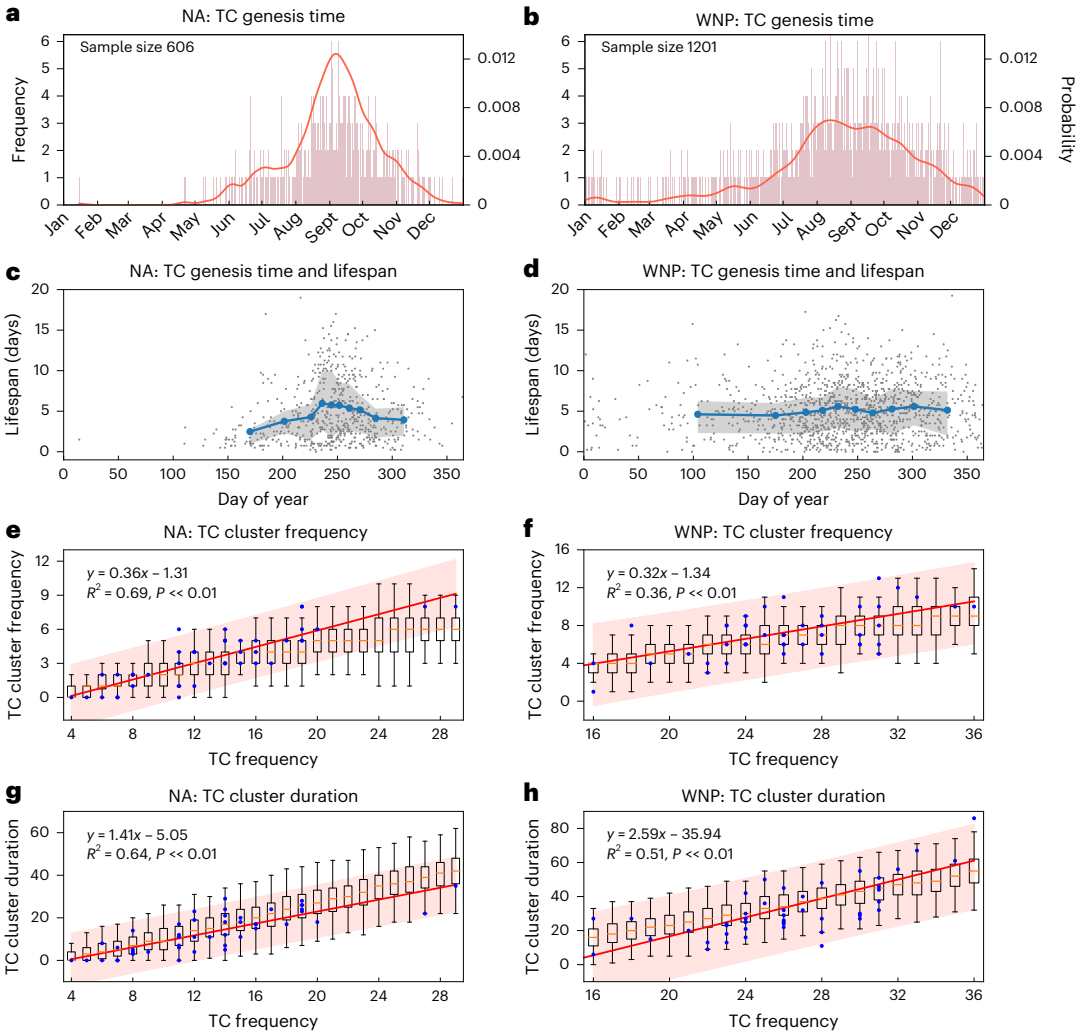

Fig. 2 | Probabilistic modelling of TC clusters. a,**b**, Histogram and PDF of TC genesis time in the NA (**a**) and WNP (**b**) derived from the 6-h best track dataset during 1979–2024. **c**,**d**, The joint distribution of TC genesis time and lifespan in the NA (**c**) and WNP (**d**). The average values of TC lifespan in every tenth percentile of TC genesis time are plotted as blue lines, and the shaded area indicates the range of the first quartile to the third quartile of the data. **e**,**f**, The relationship between yearly TC frequency and yearly TC cluster frequency in the NA (**e**) and WNP (**f**) in observations (blue dots) and 1,000 Monte Carlo simulations (box plots) during 1979–2024. **g**,**h**, The relationship between yearly TC frequency and yearly TC cluster duration in the NA (**g**) and WNP (**h**) in observations (blue dots) and 1,000 Monte Carlo simulations (box plots) during 1979–2024. Linear regressions between TC frequency and TC cluster frequency/duration in observations are shown as red lines, with 95% confidence intervals shaded on the basis of the two-tailed Student's *t*-test. The function, R^2, and *P* value ($P \ll 0.01$) of the models are presented in the top left of the figure. In each box plot, the box spans from the first quartile to the third quartile of the data, with a line marking the median. The whiskers extend from the box by 1.2× the interquartile range.

According to this framework, we can estimate TC cluster frequency and their total occurrence days (denoted as 'duration') under the assumption that TCs independently and randomly occur (Fig. 2e–h, box plots). The probabilistic model simulates the observed relationship between TC frequency and TC cluster activity quite well, with most observations (blue dots) falling within the box plots. Both the TC cluster frequency and duration increase with the TC frequency.

We further couple the probabilistic model with seven high-resolution climate models capable of resolving TC activity (CMIP6-HighResMIP; the High Resolution Model Intercomparison Project (HighResMIP) within the Coupled Model Intercomparison Project Phase 6 (CMIP6)[31,32] (Methods and Extended Data Figs. 1 and 2). Simulated TC cluster features from these full-physics high-resolution climate models align well with the estimation in the probabilistic modelling. Compared with linear regression results (red lines), the probabilistic simulations (box plots) better capture the increasing tendency from zero at a relatively low TC frequency and the saturation behaviour of TC cluster frequency at a higher TC frequency. This saturation is intrinsic to the TC cluster definition, as a high TC frequency leads to persistent overlap among multiple TCs, causing a level off or even a decline in TC cluster frequency (Extended Data Fig. 2a). Thus, TC cluster duration may serve as a better indicator of potential TC cluster hazards under high TC frequency conditions.

To further validate the model across other basins, we perform probabilistic simulations in all six major TC genesis basins on the basis of observations and the multi-model ensemble (MME) of the seven high-resolution climate models from CMIP6-HighResMIP (Extended Data Figs. 3 and 4). The TC cluster frequency and duration are well distributed in the box plots generated by Monte Carlo simulations across the six basins. This result indicates that the effect of TC climatology in frequency, lifespan and genesis time predominantly govern TC cluster climatology, and the probabilistic model can be used to decompose the relative contributions of each individual parameter to TC cluster changes.

https://doi.org/10.1038/s41558-025-02397-9

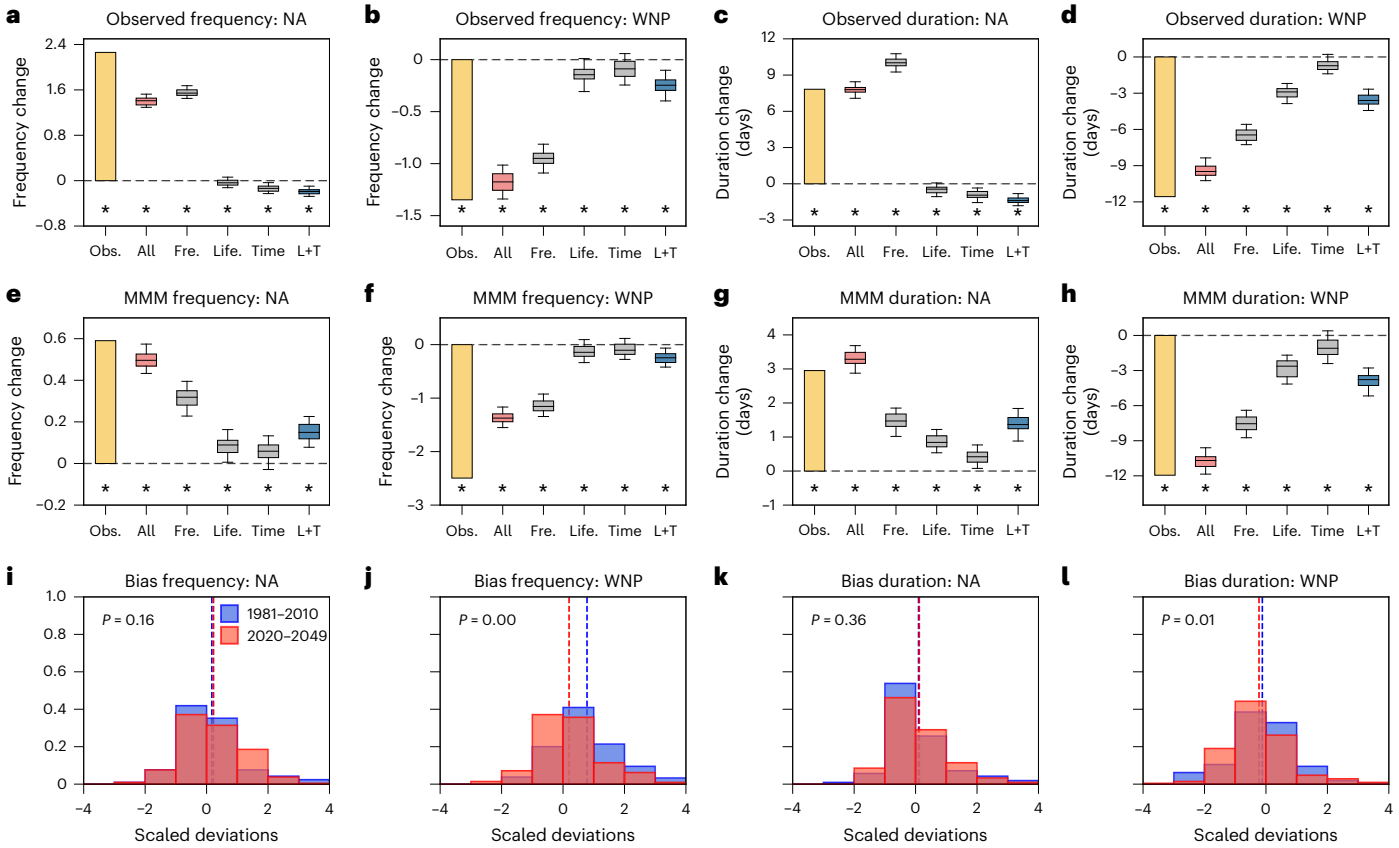

Fig. 3 | Quantifying contributions of TC climatology changes to TC cluster changes in probabilistic modelling. a,**b**, The observed TC cluster frequency change (yellow histogram) and the changes simulated by probabilistic modelling (box plots) between 1979–2001 and 2002–2024 (the latter minus the former) in the NA (**a**) and WNP (**b**). Contributions from changes in TC climatology ('All') and individual parameters ('Fre.' denotes TC frequency; 'Life.' denotes TC lifespan; 'Time' denotes TC genesis time; and 'L+T' is the combinations of TC lifespan and genesis time) are simulated by varying the given parameter(s) while keeping the other(s) fixed (Methods). The box plots show the averages of every 1,000 Monte Carlo simulations (in total, 100 averages). The box spans from the first quartile to the third quartile of the data, with a line marking the median. The whiskers represent the range from the 5th to the 95th percentile of the data. Asterisks indicate that the mean value is significantly different from zero at the 95% confidence level based on the 1,000-sample bootstrapping. **c**,**d**, The observed TC cluster duration and the changes simulated by probabilistic modelling (box plots) between 1979–2001 and 2002–2024 (the latter minus the former) in the NA (**c**) and WNP (**d**). **e**,**f**, The observed MME of seven high-resolution climate models from CMIP6-HighResMIP and the changes simulated by probabilistic modelling (box plots) between 1981–2010 and 2020–2049 (the latter minus the former) in the NA (**e**) and WNP (**f**). **i**,**j**, Deviations of average TC cluster frequency in probabilistic modelling from model outputs scaled by the standard deviation of residuals in corresponding linear regression models in the NA (**i**) and WNP (**j**) based on the MME. **k**,**l**, Deviations of average TC cluster duration in probabilistic modelling from model outputs scaled by the standard deviation of residuals in corresponding linear regression models in the NA (**k**) and WNP (**l**) based on the MME. The blue and red vertical dotted lines in **i**–**l** denote the mean bias of the probabilistic model during 1981–2010 and 2020–2049, respectively. The *P* value of the Kolmogorov–Smirnov test used to test the statistical difference between the bias distributions during the two periods is shown at the top left of **i**–**l**.

Changing TC cluster activity and its drivers

The quantitative contributions of each parameter in both the observations and model projections are presented in Fig. 3a–h and Extended Data Tables 1 and 2 (Methods). During the recent 46 years, there has been an increase in TC cluster frequency by 2.3 events and an increase in duration by 7.8 days over the NA. Conversely, the frequency of TC clusters has decreased by 1.3 events, and the duration has decreased by 11.6 days over the WNP. The contrasting changes in TC cluster activity between the NA and the WNP are projected to continue through mid-twenty first century in the MME and individual model projections[6] (Supplementary Table 1). These changes are well captured by the probabilistic modelling, except for a marked underestimation of the projected decrease in TC cluster frequency over the WNP (Fig. 3f), which explains only 54.7% of the TC cluster changes.

The bias of the probabilistic model arises from both model uncertainty and systematic error, with the latter due to assuming that TCs in clusters are generated independently. Intense TCs can induce alternating cyclonic and anti-cyclonic disturbances, as observed in 2004 over the WNP (Fig. 1b), leading to subsequent TCs in the wake of pre-existing TCs[12]. Such dynamic processes, involving enhanced synoptic wave trains, are favourable for TC cluster formation[5,22,24,33], contributing to the systematic underestimation of TC cluster frequency in the probabilistic model (Fig. 3i,j). In contrast to TC cluster frequency, the bias distribution of TC cluster duration does not show a robust positive shift from zero in the mean value (Fig. 3k,l), probably owing to damping effects by the randomized TC lifespan. Especially, the bias distribution for TC cluster frequency over the WNP (Fig. 3j) exhibits statistically significant differences between the future (2020–2049) and historical (1981–2010) periods, as shown by the Kolmogorov–Smirnov test ($P < 0.01$), which mainly stems from a shift in the model's mean bias. This significant shift can partially explain the probabilistic model's failure to simulate the projected decrease in TC cluster frequency over the WNP (Fig. 3f). The physical processes underlying this discrepancy are investigated in the following section.

An increase in TC frequency can directly enhance TC cluster activity, as shown in Fig. 2e,f. The TC seasonality and lifespan influence

https://doi.org/10.1038/s41558-025-02397-9

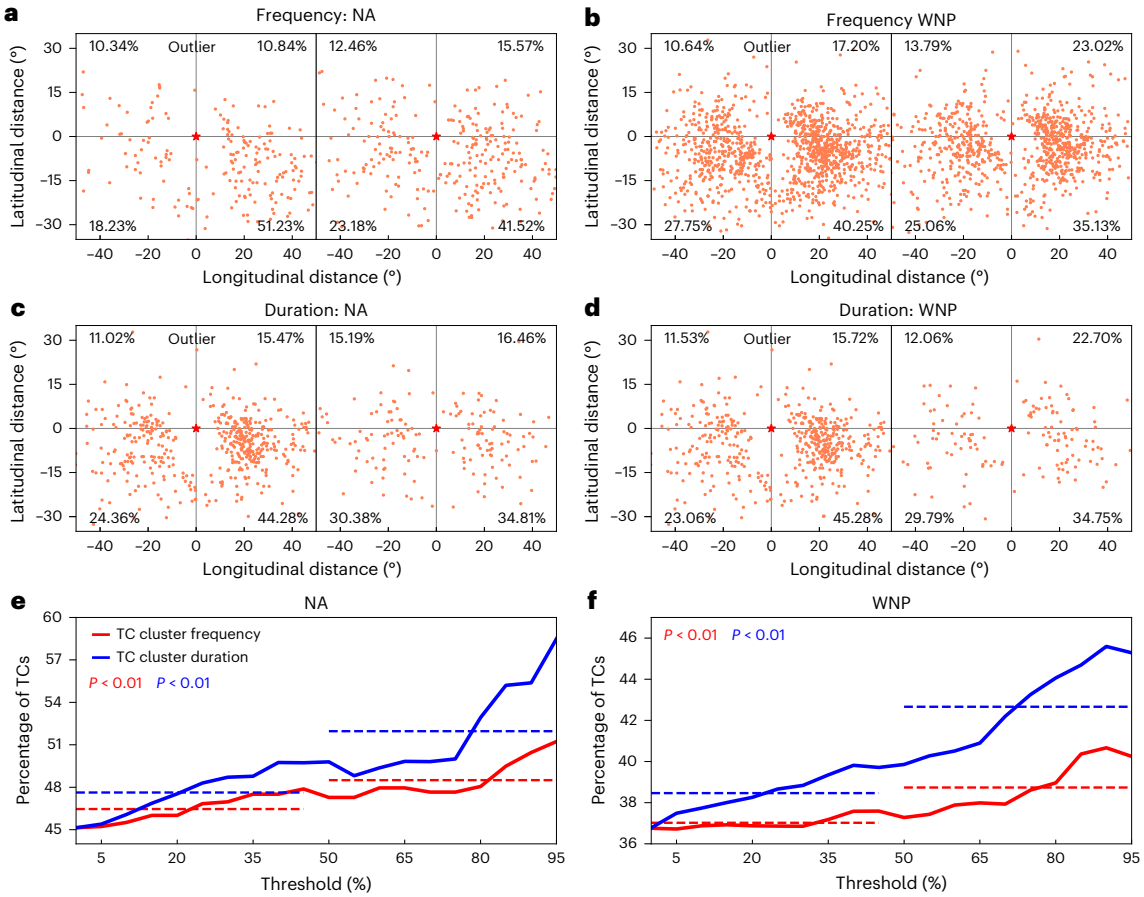

Fig. 4 | Identification of dynamically connected TC clusters. a,**b**, The relative locations between pre-existing TCs (red star) and subsequent TCs (orange dots) at the cyclogenesis time of the subsequent TCs in the outlier group (left) and normal group (right) categorized by TC cluster frequency in the NA (**a**) and WNP (**b**) based on the MME of the highresSST-present simulation in seven high-resolution climate models from CMIP6-HighResMIP during 1950–2014. **c**,**d**, The relative locations between pre-existing TCs (red star) and subsequent TCs (orange dots) at the cyclogenesis time of the subsequent TCs in the outlier group (left) and normal group (right) categorized by TC cluster duration in the NA (**c**) and WNP (**d**) based on the MME of the highresSST-present simulation in seven high-resolution climate models from CMIP6-HighResMIP during 1950–2014. Percentages of subsequent TCs in each quadrant are indicated in the four corners. Considering wave energy dispersion for limited distance, our analysis focusses on a region extending 35° north and south in latitude and 50° east and west in longitude from each pre-existing TC. **e**,**f**, The percentages of subsequent TCs located in the southeastern quadrant with different percentile thresholds to define the outlier group in the NA (**e**) and WNP (**f**), categorized by TC cluster frequency (red lines) and TC cluster duration (blue lines) (Methods). The average ratios between the two regimes, separated by a threshold of 50%, are plotted as dotted lines. The mean ratios between the two stages (TC cluster frequency and TC cluster duration) are statistically different with $P < 0.01$ based on the 1,000-sample bootstrapping.

the TC cluster activity by modulating the genesis time interval and the likelihood of overlap between TCs, respectively. In general, the TC frequency change is the primary contributor to the TC cluster change, explaining 46.0–128.4% of the TC cluster changes (Fig. 3a–h and Extended Data Tables 1 and 2). Changes in the TC lifespan and seasonality play a secondary role in regulating the TC cluster activity over time. Observed changes in the TC lifespan and seasonality lead to a 8.5% reduction in the TC cluster frequency and a 17.5% reduction in the TC cluster duration over the NA. These results may be due to the recent increase in short-lived TCs over the NA[19]. The probabilistic model explains a larger portion of the changes in TC cluster activities when focussing on relatively long-lived TCs (lasting ≥2 days; Extended Data Fig. 5).

Note that the relationship between TC lifespan and genesis time may introduce additional complexity. However, our decomposition results show that the contributions of collaborate changes in TC lifespan and seasonality can be linearly reconstructed on the basis of each parameter's individual contribution (Extended Data Tables 1 and 2, the last three columns), thereby enhancing our confidence in the results within the probabilistic framework.

Identification of dynamically connected TC clusters

In the Northern Hemisphere, TCs typically move northwestward owing to climatological steering flow and the Beta effect[34]. If a TC is pre-conditioned by a Rossby wave train or other synoptic-scale disturbance linked to a pre-existing TC; the genesis location of this new TC will most probably be in the southeastern quadrant relative to the pre-existing one because of the wave energy dispersion under easterly vertical wind shear[4,5,24]. We evaluate the likelihood of a new TC formation southeast of the pre-existing TC against the random probabilistic framework to identify dynamically connected TC clusters.

We begin by comparing the spatial distribution of newly formed TCs relative to pre-existing TCs in the outlier group and the normal group (Methods). Outliers are defined as TC clusters with yearly frequency or duration (for example, blue dots in Fig. 2e) that is above the 95th percentile of the Monte Carlo simulations (for example, box plots in Fig. 2e), while events positioned at the median value of the Monte Carlo simulations are categorized as the normal group. In both groups, the largest proportion of TCs is located in the southeastern quadrant of the pre-existing TCs because of the general west-polewards

https://doi.org/10.1038/s41558-025-02397-9

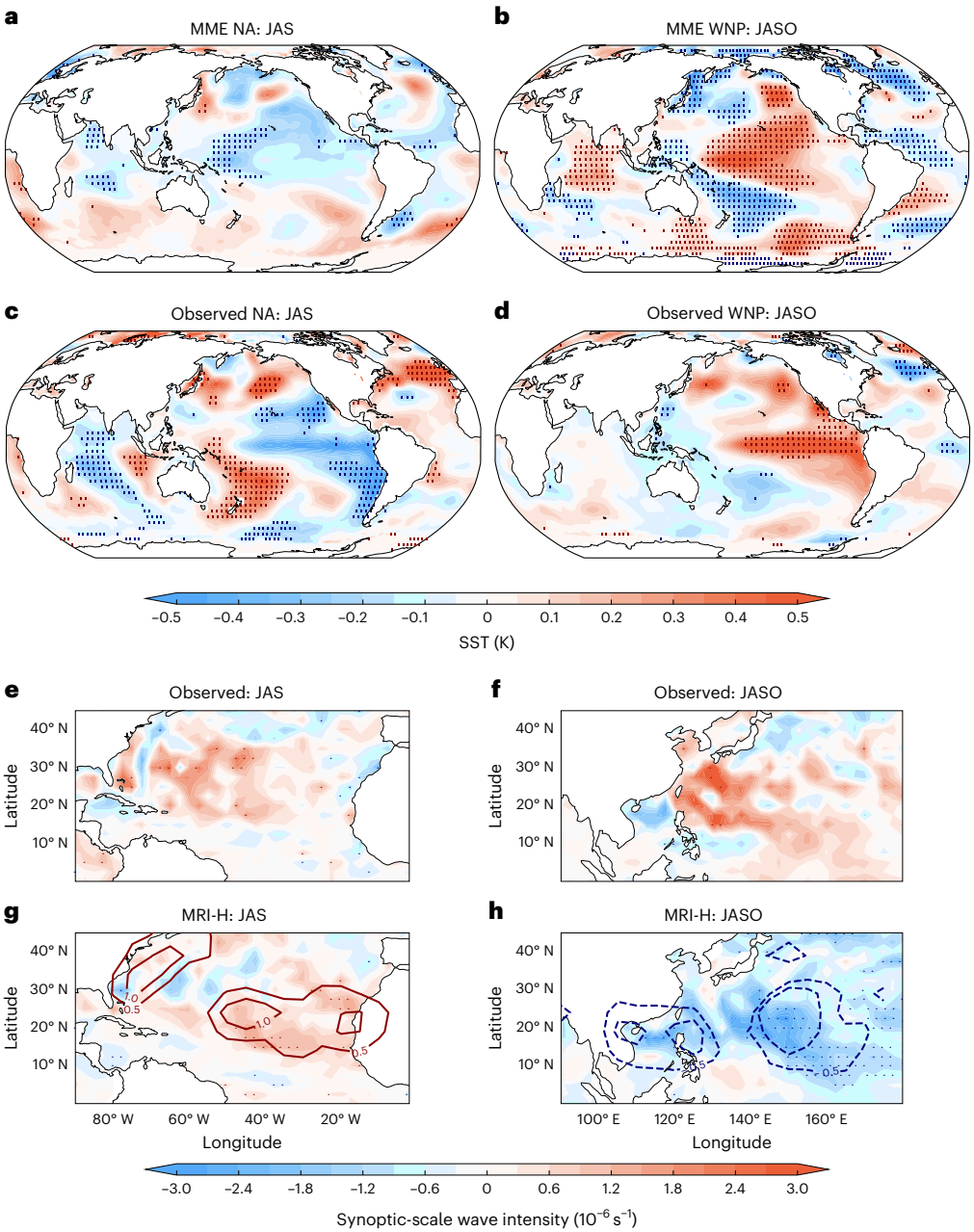

Fig. 5 | Patterns of SST and synoptic-scale wave activity that are favourable for dynamically connected TC clusters. a,**b**, The composite differences in SST (K) between TC cluster outlier group and normal group during 1950–2014 based on the MME of the highresSST-present simulations from CMIP6-HighResMIP. To isolate the dynamically connected TC clusters from randomly generated events, the normal and outlier groups are categorized by the 15th and 95th percentile of TC cluster frequency based on the probabilistic modelling in the NA (**a**) and WNP (**b**) (Methods). **c**,**d**, The composite differences in SST (K) between TC cluster outlier group and normal group based on observational data, with two groups divided by the 50th percentile of TC cluster frequency during 1979–2024 to ensure a sufficient and comparable sample size for the two groups, in the NA (**c**) and WNP (**d**). **e**,**f**, The differences in synoptic-scale wave intensity (10^{-6} s^{-1}) between TC cluster outlier group and normal group based on observational data during 1979–2024, with two groups divided by the 50th percentile of TC cluster frequency, over the NA (**e**) and WNP (**f**). **g**,**h**, Effects of long-term La Niña-like warming in the tropical Pacific on synoptic-scale wave activity (shading) and TC track density (contour) in the MRI-AGCM3-2-H experiments in the NA (**g**; (0.5, 1) red contours) and WNP (**h**; (−1.5, −0.5) blue contours). As the SST trend in the experiments between the periods 1981–2010 and 2020–2049 shows a cooling in the tropical Pacific (Extended Data Fig. 7), the differences in synoptic-scale wave intensity and TC track density are considered to be forced by La Niña-like global warming pattern. The averages of changes are shown for TC peak seasons in each basin (that is, JAS for the NA and JASO for the WNP). In all panels, the dots indicate statistically significant differences at a 95% confidence interval based on the 1,000-sample bootstrapping and false discovery rate test. Basemaps from Natural Earth (https://www.naturalearthdata.com).

propagation of TCs (Fig. 4a–d). Notably, however, a higher concentration of TCs is observed within this quadrant in the outlier groups in both the NA and WNP, with ratios increasing by 10.53% and 5.12%, respectively. These results suggest that the increased TC ratio in the wake of pre-existing TCs (that is, the southeastern quadrant) is probably associated with active dynamic connections between TCs. The enhanced activity of synoptic-scale wave trains may lead to an underestimation by the probabilistic model. Similar conclusions are drawn from observational data, except for results categorized by TC cluster duration over the WNP (Supplementary Fig. 2).

To validate robustness of the contribution from dynamic connections, we gradually increase the threshold used to define outliers from the 0th to the 95th percentile (Methods) and investigated the changes in TC ratio in the southeastern quadrant (Fig. 4e,f). The ratios remain nearly unchanged at lower percentile thresholds and rapidly increase once the threshold reaches the 70th percentile. Ratios calculated on the basis of data below the 50th percentile are significantly different from those in the second half, indicating a robust signal of dynamic connections. Previous attempts to detect dynamically connected events by comparing differences between TC clusters conditions with a climatological base state[12,33] and single TC conditions[5,24] suffer from an inaccurate baseline, while numerical case studies[29,30] are limited by insufficient sample sizes. Our study sidesteps these issues, presenting a more accurate baseline from the probabilistic model with adequate samples based on the MME with seven full-physics climate model simulations. Systematic deviations from this baseline arise from neglecting dynamically connected events. This approach identifies the role of dynamic connections in TC clusters and their underlying physical drivers as demonstrated below.

Shifting hotspot driven by the surface warming pattern

Local and remote SST forcings modulate synoptic-scale wave variability through large-scale circulations[12,35,36] (Methods). We investigate the SST patterns that favour dynamic connections between TCs (Fig. 5a–d and Methods). The enhanced dynamic connections between TCs over the WNP and NA are associated with El Niño and La Niña conditions, as evidenced by both climate model simulations and observations (Fig. 5a–d). Observational composites of synoptic-scale wave intensity for the corresponding groups of years (categorized into outlier years and normal years) support the linkage between dynamically connected TC clusters and enhanced synoptic disturbance activity (Fig. 5e,f and Supplementary Fig. 3 for validation in another reanalysis). Synoptic-scale wave activities strengthened over the broad subtropical NA, while synoptic-scale wave intensity anomalies are characterized by a northwest–southeast-oriented band in the WNP. In these regions with large zonal wind shear, synoptic-scale wave trains can develop by converting barotropic energy from the mean flow[13]. Similar patterns are observed when composites are grouped on the basis of TC cluster duration (Supplementary Fig. 4).

La Niña events can increase TC frequency in the NA by reducing the vertical wind shear[37,38], whereas they primarily redistribute TC genesis locations in the WNP with a slight decrease in TC frequency[39,40]. In addition to direct TC frequency changes, we show that the contrasting effects of ENSO on TC cluster frequency and duration over the two basins can be further reinforced by changes in dynamically connected events, especially for the WNP. The lower Kendall rank correlation between TC frequency and TC cluster frequency over the WNP, compared with the NA, also confirms the weaker influence of TC climatology features on TC cluster formation in this basin (Fig. 1c,d).

Recent decades have witnessed a cooling trend over the tropical Pacific, known as La Niña-like warming[41]. While it is known that interannual ENSO causes seesaw changes in TC cluster activity between the two basins, the impacts of La Niña-like global warming pattern on TC cluster activity need to be further qualified. We take daily outputs of the highresSST-present and highresSST-future simulations from MRI-AGCM3-2-H, whose results show good agreement with the MME in projected changes in TC clusters over the NA and WNP (Supplementary Table 1). As the forced warming pattern between the two periods (1981–2010 and 2020–2049) after tropical mean warming rate subtracted is similar to the observed cooling in tropical Pacific (Extended Data Fig. 6), the differences in synoptic-scale wave intensity are taken as the responses to the recent La Niña-like global warming pattern (Fig. 5g,h). The synoptic-scale wave intensity is projected to increase across the NA (Fig. 5g), indicative of enhanced dynamic connections. Meanwhile, there is a significant decrease in synoptic-scale wave intensity over the mean flow confluence regions in the WNP (Fig. 5h), indicating that the La Niña-like global warming pattern will lead to suppression of the dynamically connected TC clusters over the WNP by reducing barotropic energy conversion. In addition, the widespread increase and decrease synoptic-scale wave intensity over the two basins agree well with TC track density changes (Fig. 5g,h), suggesting contrasting trends in TC frequency by changes in pre-TC synoptic-scale disturbances, which are typically referred to as 'TC seeds'[35,42–44]. Observational evidence confirms that the increase in TC frequency over the NA and decrease over WNP are associated with tropical Pacific cooling and warming elsewhere, including the positive Atlantic Multidecadal Oscillation (AMO)-like anomalies[45–48] (Extended Data Fig. 7). These results, together with findings in Fig. 5e–h, suggest that long-term La Niña-like global warming pattern (Extended Data Fig. 6) contributes to contrasting changes in TC clusters over the NA and WNP in both observations and model projections through modulating TC frequency and synoptic-scale wave intensity.

The above analysis shows that changes in synoptic-scale wave intensity driven by the recent La Niña-like global warming pattern can further increase (decrease) dynamically connected TC cluster activity over the NA (WNP), leading to a systematic bias in the probabilistic model (Fig. 3i–k). The significant decrease in model bias in projected TC cluster frequency in the WNP is closely related to the suppression of dynamically connected events under forced La Niña-like warming conditions (Fig. 3j).

Discussion

We have developed a probabilistic model to investigate changes in TC cluster activity over the NA and WNP and disentangle the individual contributions of changes in TC climatology features to TC cluster changes. This model is used as a baseline for random occurring independent TCs, against which we identify outliers as dynamically connected TC clusters. We reveal that the NA has recently emerged as a TC cluster hotspot owing primarily to the increased TC frequency and dynamically connected TC clusters driven by the recent La Niña-like global warming pattern. Whether this warming pattern is internally generated or externally forced remains an open question and warrants further investigations. Nonetheless, we find that the contrasting trends in TC cluster frequency between the NA and WNP remain robust even when the study period is extended to 1961 (Supplementary Fig. 5), suggesting the presence of a long-term change signal that goes beyond the impacts of inter-decadal variability. We perform a suite of high-resolution climate model experiments with different global warming patterns to test the hypothesis (Methods). When forced with the observed La Niña-like global warming pattern over 1960–2014, the hotspot for TC clusters shifts from the WNP to the NA basin (Extended Data Fig. 8). When forced with the projected El Niño-like warming, the TC cluster activities are suppressed in both basins, with a larger decrease occurring over the WNP.

Estimated based on TC climatology feature changes, the possibility for TC cluster frequency over the NA to exceed that of the WNP has sharply increased by as much as tenfold from 1.4 ± 0.4% to 14.3 ± 1.2% over the past 46 years (Methods). With the ongoing Pacific decadal cooling, this likelihood will further increase when changes in dynamically connected TC clusters are considered, highlighting a rapidly growing TC cluster threat to the coastal NA.

Investigating systematic biases in probabilistic modelling based on seven full-physics high-resolution climate models, we robustly identify the role of enhanced synoptic-scale wave intensity in dynamically connected TC clusters. However, quantifying this contribution from dynamically connected events remains a challenge and should be further pursued. Regardless, our research highlights the importance of TC clusters for hazard assessment, which often assumes independent TC events. Future research could explore more sophisticated modelling to explicitly capture dynamic interactions within TC clusters and

investigate the landfall phase of TC clusters to support hazard assessment frameworks towards better representation of such temporally compound events.

Online content

Any methods, additional references, Nature Portfolio reporting summaries, source data, extended data, supplementary information, acknowledgements, peer review information; details of author contributions and competing interests; and statements of data and code availability are available at https://doi.org/10.1038/s41558-025-02397-9.

References

1. National Centers for Environmental Information. *Monthly Tropical Cyclones Report for September 2020* (NOAA NCEI, 2020).
2. Xi, D., Lin, N. & Gori, A. Increasing sequential tropical cyclone hazards along the US East and Gulf coasts. *Nat. Clim. Change* **13**, 258–265 (2023).
3. Xi, D. & Lin, N. Sequential landfall of tropical cyclones in the United States: from historical records to climate projections.*Geophys. Res. Lett.* **48**, e2021GL094826 (2021).
4. Sun, X. & Xie, L. A climatological study of successive tropical cyclone events in North Atlantic. *Atmosphere* **13**, 1909 (2022).
5. Schenkel, B. A climatology of multiple tropical cyclone events. *J. Clim.* **29**, 4861–4883 (2016).
6. Fu, Z.-H. et al. Future projections of multiple tropical cyclone events in the Northern Hemisphere in the CMIP6-HighResMIP models. *Geophys. Res. Lett.* **50**, e2023GL103064 (2023).
7. Zscheischler, J. et al. Future climate risk from compound events. *Nat. Clim. Change* **8**, 469–477 (2018).
8. Zscheischler, J. et al. A typology of compound weather and climate events. *Nat. Rev. Earth Environ.* **1**, 333–347 (2020).
9. Matthews, T., Wilby, R. L. & Murphy, C. An emerging tropical cyclone–deadly heat compound hazard. *Nat. Clim. Change* **9**, 602–606 (2019).
10. Sullivan, L. & Schwartz, E. *FEMA Report Acknowledges Failures in Puerto Rico Disaster Response* (National Public Radio, 2018).
11. Kim, J.-H., Ho, C.-H. & Sui, C.-H. Circulation features associated with the record-breaking typhoon landfall on Japan in 2004. *Geophys. Res. Lett.* **32**, L14713 (2005).
12. Hu, K. et al. A train-like extreme multiple tropical cyclogenesis event in the northwest Pacific in 2004. *Geophys. Res. Lett.* **45**, 8529–8535 (2018).
13. Gao, J. & Li, T. Interannual variation of multiple tropical cyclone events in the western North Pacific. *Adv. Atmos. Sci.* **29**, 1279–1291 (2012).
14. Emanuel, K. A. Downscaling CMIP5 climate models shows increased tropical cyclone activity over the 21st century. *Proc. Natl Acad. Sci. USA* **110**, 12219–12224 (2013).
15. Chand, S. S. et al. Declining tropical cyclone frequency under global warming. *Nat. Clim. Change* **12**, 655–661 (2022).
16. Shan, K. et al. Seasonal advance of intense tropical cyclones in a warming climate. *Nature* **623**, 83–89 (2023).
17. Truchelut, R. E. et al. Earlier onset of North Atlantic hurricane season with warming oceans. *Nat. Commun.* **13**, 4646 (2022).
18. Feng, X., Klingaman, N. P. & Hodges, K. I. Poleward migration of western North Pacific tropical cyclones related to changes in cyclone seasonality. *Nat. Commun.* **12**, 6210 (2021).
19. Klotzbach, P. J. et al. Trends in global tropical cyclone activity: 1990–2021. *Geophys. Res. Lett.* **49**, e2021GL095774 (2022).
20. Landsea, C. W. et al. Impact of duration thresholds on atlantic tropical cyclone counts. *J. Clim.* **23**, 2508–2519 (2010).
21. Ritchie, E. A. & Holland, G. J. Large-scale patterns associated with tropical cyclogenesis in the Western Pacific. *Mon. Weather Rev.* **127**, 2027–2043 (1999).
22. Yoshida, R. & Ishikawa, H. Environmental factors contributing to tropical cyclone genesis over the Western North Pacific. *Mon. Weather Rev.* **141**, 451–467 (2013).
23. Krouse, K. D., Sobel, A. H. & Polvani, L. M. On the wavelength of the rossby waves radiated by tropical cyclones. *J. Atmos. Sci.* **65**, 644–654 (2008).
24. Krouse, K. & Sobel, A. An observational study of multiple tropical cyclone events in the western north Pacific. *Tellus A* **62**, 256–265 (2010).
25. Lau, K.-H. & Lau, N.-C. Observed structure and propagation characteristics of tropical summertime synoptic scale disturbances. *Mon. Weather Rev.* **118**, 1888–1913 (1990).
26. Murakami, H. et al. Future changes in tropical cyclone activity projected by the new high-resolution MRI-AGCM. *J. Clim.* **25**, 3237–3260 (2012).
27. Dickinson, M. & Molinari, J. Mixed Rossby–gravity waves and Western Pacific tropical cyclogenesis. Part I: synoptic evolution. *J. Atmos. Sci.* **59**, 2183–2196 (2002).
28. Frank, W. M. & Roundy, P. E. The role of tropical waves in tropical cyclogenesis. *Mon. Weather Rev.* **134**, 2397–2417 (2006).
29. Li, T. et al. Tropical cyclogenesis associated with Rossby wave energy dispersion of a preexisting typhoon. Part II: numerical simulations. *J. Atmos. Sci.* **63**, 1390–1409 (2006).
30. Wu, Y. & Chan, K. T. F. Subsequent tropical cyclogenesis in the South China Sea induced by the pre-existing tropical cyclone over the western North Pacific: a case study. *Front. Earth Sci.* **11**, 1235748 (2023).
31. Eyring, V. et al. Overview of the Coupled Model Intercomparison Project Phase 6 (CMIP6) experimental design and organisation. *Geosci. Model Dev.* **9**, 1937–1958 (2016).
32. Roberts, M. J. et al. Impact of model resolution on tropical cyclone simulation using the HighResMIP-PRIMAVERA multi-model ensemble. *J. Clim.* **33**, 2557–2583 (2020).
33. Schenkel, B. Are multiple tropical cyclone events similar among basins? *J. Clim.* **30**, 5805–5813 (2017).
34. Holland, G. J. Tropical cyclone motion: environmental interaction plus a beta effect. *J. Atmos. Sci.* **40**, 328–342 (1983).
35. Vecchi, G. A. et al. Tropical cyclone sensitivities to CO_2 doubling: roles of atmospheric resolution, synoptic variability and background climate changes. *Clim. Dyn.* **53**, 5999–6033 (2019).
36. Wu, R., Wang, Y. & Cao, X. What modulates the intensity of synoptic-scale variability over the western North Pacific during boreal summer and fall? *J. Clim.* **34**, 3645–3662 (2021).
37. Gray, W. M. Atlantic seasonal hurricane frequency. Part I: El Niño and 30 mb quasi-biennial oscillation influences. *Mon. Weather Rev.* **112**, 1649–1668 (1984).
38. Smith, D. M. et al. Skilful multi-year predictions of Atlantic hurricane frequency. *Nat. Geosci.* **3**, 846–849 (2010).
39. Wang, B. & Chan, J. C. L. How strong ENSO events affect tropical storm activity over the Western North Pacific. *J. Clim.* **15**, 1643–1658 (2002).
40. Zhan, R., Wang, Y. & Lei, X. Contributions of ENSO and East Indian Ocean SSTA to the interannual variability of Northwest Pacific tropical cyclone frequency. *J. Clim.* **24**, 509–521 (2011).
41. Watanabe, M. et al. Possible shift in controls of the tropical Pacific surface warming pattern. *Nature* **630**, 315–324 (2024).
42. Yoshimura, J., Sugi, M. & Noda, A. Influence of greenhouse warming on tropical cyclone frequency. *J. Meteorol. Soc. Jpn Ser. II* **84**, 405–428 (2006).
43. Sugi, M. et al. Future changes in the global frequency of tropical cyclone seeds. *SOLA* **16**, 70–74 (2020).
44. Yamada, Y. et al. Evaluation of the contribution of tropical cyclone seeds to changes in tropical cyclone frequency due to global warming in high-resolution multi-model ensemble simulations. *Prog. Earth Planet. Sci.* **8**, 11 (2021).

45. Wang, C. et al. A seesaw variability in tropical cyclone genesis between the western North Pacific and the North Atlantic shaped by Atlantic multidecadal variability. *J. Clim.* **35**, 2479–2489 (2022).
46. Chan, J. C. L. & Liu, K. S. Recent decrease in the difference in tropical cyclone occurrence between the Atlantic and the western North Pacific. *Adv. Atmos. Sci.* **39**, 1387–1397 (2022).
47. Zhao, J. et al. Lapsed El Niño impact on Atlantic and Northwest Pacific tropical cyclone activity in 2023. *Nat. Commun.* **15**, 6706 (2024).
48. Huang, H. et al. Contrasting responses of Atlantic and Pacific tropical cyclone activity to Atlantic multidecadal variability. *Geophys. Res. Lett.* **50**, e2023GL102959 (2023).

Methods

Probabilistic TC cluster model

To statistically analyse the climatology of TC clusters, we design a probabilistic TC cluster model based on a probabilistic TC occurrence model developed from refs. 2,3. Within this modelling framework, we do not account for the dynamic connections between TCs in a TC cluster; that is, the occurrence of each TC is assumed to be independent of the occurrence of the others. Thus, the probabilistic model can serve as a TC cluster baseline contributed by randomly occurring independent TCs. The deviations from this baseline can be used to identify the dynamically connected TC clusters.

The model consists of three parameters, namely the annual basin-wide TC genesis frequency n, the date of TC genesis T and the TC lifespan D. Here the genesis frequency n is a deterministic value either obtained from historical observations and simulations or prescribed as a given value, while the genesis date T and the duration D of each of the n TCs are considered to be random variables. The genesis date and duration of TCs are shown to be correlated (Fig. 2c,d). However, limited historical observations and climate simulations prevent a robust estimation of the joint probability distribution of the two variables. Instead, we first obtain the kernel density estimations (KDE) of TC genesis time T. Then, we bin every tenth percentile of T and obtain the conditional PDF of TC lifespan D for each bin of T using the KDE. The estimation is performed for historical observations in each basin, and for two periods (1950–2014 and 2015–2050) for each climate model simulation.

For each year, with a fixed number of TCs, we apply the KDE of T and the conditional KDE of D to perform 1,000 Monte Carlo simulations of the genesis date and duration of TCs in that year. In each Monte Carlo simulation, when two or more TCs co-exist simultaneously, we count it as one TC cluster event (frequency) and document the duration of the co-existence as the duration of the TC cluster (days). The simulated TC cluster frequency and duration of the 1,000 Monte Carlo members are used to represent the climatology of the TC cluster.

Decomposing the contribution to TC cluster changes from TC climatology features

The abovementioned probabilistic model enables the flexibility to investigate the influence of the change in each individual feature of TC climatology on changes in the frequency and duration of TC cluster activity. We perform sensitivity tests to decompose the impact from genesis frequency n ('Fre.'), date of TC genesis T ('Time') and TC lifespan D ('Life') individually, as well as the joint impact from the changes in T and D together ('L + T') on TC cluster changes. To study the individual influences in MME, we change one parameter at a time from its historical probability distribution during 1981–2010 to its future probability distribution during 2020–2049 estimated from climate model outputs, while keeping the other parameters the same as their historical values. We also investigate the individual influence of the changes in observations between 1979–2001 and 2002–2024. We repeat these sensitivity experiments 100 times (that is, 100,000 simulations in total) for every parameter to obtain statistically robust results. The differences between the estimated probability distributions of the simulated TC cluster frequency or duration and the historical probability distributions are used to represent the influence of the selected parameter(s). To estimate the change in the possibility of NA TC cluster frequency exceeding that of the WNP in observations, we compare the simulated TC cluster frequency over the NA and WNP in the two periods (1979–2001 and 2002–2024) by the probabilistic model. The possibility is calculated as the percentage of instances where the TC cluster frequency over the NA surpasses that of the WNP.

Observational data

TC best-track data are obtained from the International Best Track Archive for Climate Stewardship (IBTrACS)[49], which is compiled by six Regional Specialized Meteorological Centres and four Tropical Cyclone Warning Centres affiliated with the World Meteorological Organization. We use 6-h TC records for the period of 1979–2024 in the NA and WNP, as data quality before 1979 is poor owing to the absence of routinely used geostationary satellites for monitoring. Thus, pre-1979 records should be interpreted with caution owing to observational limitations. Nevertheless, extending the TC dataset to the 1950s will not alter the contrasting TC cluster trends between the NA and WNP (Supplementary Fig. 5). TC records from 1979 to 2022 are also analysed for the other four basins: the East Pacific, North Indian, South Indian and South Pacific. Since our focus is on TC genesis and its persistence in a basin rather than its intensity—a parameter that suffers from substantial uncertainty[50]—our probabilistic model results are not sensitive to the dataset selection. We considered only TCs that reached at least tropical storm intensity (≥35 kt) during their lifetime. However, our conclusions remain unchanged when tropical depressions, extratropical cyclones and subtropical storms are included (Supplementary Fig. 6).

Monthly SST data are obtained from the Extended Reconstructed Sea Surface Temperature version 5 (ERSST.v5)[51] during 1950–2024. To calculate synoptic-scale wave intensity, we use 6-h zonal and meridional wind data at 850 hPa during 1979–2024 based on the fifth-generation atmospheric reanalysis from the European Centre for Medium-Range Weather Forecasts (ERA5)[52]. We also analyse the results using daily reanalysis data from the National Centres for Environmental Prediction–Department of Energy (NCEP/DOE Reanalysis II) during 1979–2020. Consistent with the findings from ERA5, the synoptic-scale wave intensity patterns exhibit a northwest–southeast oriented enhanced band over the WNP and a uniformly enhanced band over the NA in the NCEP/DOE dataset (Supplementary Fig. 3). We exclude the linear trends of the data to eliminate the possible influence of global warming when investigating the favourable SST pattern for dynamically connected TC clusters.

High-resolution climate simulations

The CMIP6-HighResMIP initiative uses a multi-model framework to evaluate the regional impacts of climate change on TC activity[53]. In this study, we analyse tier 1 and tier 3 simulations from seven high-resolution climate models: CNRM-CM6-1-HR[54], EC-Earth3P-HR[55], HadGEM3-GC31-HM[56], MRI-AGCM3-2-S[57], MRI-AGCM3-2-H[57], NICAM16-8S[58] and NICAM16-7S[58] (detailed in Supplementary Table 2). Coupled models are not included, as they are limited in simulating the observed warming pattern and generally perform poorly in reproducing TC climatology and the observed interannual variability of TC activity.[59,60]. Tier 1 comprises atmosphere-only simulations forced by observed daily SST and sea ice concentration from HadISST2 spanning 1950–2014 (referred to as 'highresSST-present'). Tier 3 extends tier 1 simulations through 2049 or 2050, with an option to continue to 2100 under scenario SSP585 (referred to as 'highresSST-future'). For tier 3, SST forcing incorporates the local warming rates derived from an ensemble mean of CMIP5 RCP8.5 simulations and includes interannual variability from observational data. Model resolutions are set at 50 km or finer to capture key statistics of TC climate and variability, such as genesis frequency, spatial distribution and intensity[32]. Original TC tracks are identified by the TRACK algorithm in ref. 61, which detects TCs by tracking vorticity features on a common T63 spectral grid and accounting for warm-core criteria and storm lifespan. We focus on the first ensemble member from each model and compare the differences between 1981–2010 and 2020–2049 on the basis of the MME results.

As HighResMIP simulations do not provide the SST variable online, we use variable surface air temperature (SAT) as a substitute[6] to show long-term changes in SST patterns. To ensure data reliability, we assess the Niño3.4 index derived from both observed SST and SAT in the highresSST-present simulation spanning 1979–2014 (Supplementary Fig. 7). The high correlation coefficient between the indices suggests that the SAT serves as a reliable proxy for SST.

The SST patterns in Fig. 5a,b are composited on a year-to-year timescale without any trend information, and therefore the intensified synoptic-scale wave in the dynamic connections cannot be directly attributed to the decadal SST warming pattern in the tropical Pacific (Extended Data Fig. 6). To confirm the effects of surface warming patterns on dynamically connected events, we use daily outputs from the MRI-AGCM3-2-H model to calculate the changes in synoptic-scale wave intensity. This model has good agreement with the MME in projected changes in the NA and WNP (Supplementary Table 1). In highresSST-future simulations, the model is forced by patterned warming from an ensemble mean of CMIP5 to 2050 plus observed interannual variability. The differences between the periods 1981–2010 and 2020–2049 are a La Niña-like warming pattern after the tropical mean warming rate is subtracted (shown in Extended Data Fig. 6a,b). Therefore, the changes in synoptic-scale wave intensity between the two chosen periods can be considered as the responses to La Niña-like global warming patterns.

Constraint detection for simulated TC tracks

In this study, we define TC track density at a grid point with a 1° resolution as the number of TCs passing through a 15° longitude × 15° latitude area centred at that grid point. We select a 15° × 15° box to capture synoptic waves (such as equatorial Rossby waves, mixed Rossby–gravity waves and easterly waves) that could trigger TC genesis[62].

The simulated global distribution of TC track density without constraints is shown in Supplementary Fig. 8a, which shows large overestimations, particularly in the WNP, North Indian and Southern Hemisphere. These overestimations stem from uniform detection parameters and wind speed thresholds, leading to excessive TC frequency in very-high-resolution climate models[6]. To mitigate the bias and ensure equitable representation of each model in the MME, we implement additional constraints on the basis of the TRACK algorithm, detailed in Supplementary Table 2. Owing to the different parameterization schemes used in simulating the planetary boundary layer, some high-resolution models tend to artificially reach very strong wind speeds (such as NICAM16-8S and NICAM16-7S)[63]. We increase the wind speed thresholds in these models since our focus is TC frequency rather than intensity. Furthermore, we use a relatively weak constraint on lifespan to retain short-lived TCs, which might become more prevalent in the future[19]. Besides the traditional wind speed and duration criteria, we further filter out storms generated in the region where climatological SST is lower than 26 °C, which are often misinterpreted as TCs in the TRACK algorithm[64].

The bias of TC track density is largely reduced after the constraint detection methods are implemented, although an overabundance of TCs persists in the NI, probably owing to the misidentification of monsoonal low-pressure systems[65,66] (Supplementary Fig. 8b,c). TC frequency across six basins agrees better with the observations, particularly for the WNP. Additionally, the standard deviations of TC frequency in the MME are reduced to levels comparable to the observations, indicative of the improvement of the constrained results (Supplementary Table 3).

Outlier analysis

The observed and simulated TC cluster frequencies and durations (Fig. 2e–h, blue dots) that exceed the 95th percentile of the respective Monte Carlo simulations (box plots) are defined as outliers. To maintain an adequate sample size, events falling within the 5th to 95th percentiles of the simulations are included in the normal group for comparison with the outlier group, as depicted in Supplementary Fig. 2. In the Monte Carlo simulations based on climate model outputs, events positioned at the median value of the box plots are considered as the normal group for comparison (Fig. 4a–d), ensuring a comparable sample size with outlier groups.

We investigate the relative locations between pre-existing TCs and subsequent TCs within TC clusters and quantify the TC ratio in each quadrant. The wave energy dispersion in synoptic trains cannot extend beyond 5,000 km owing to its decaying feature and basin size[67], and thus we only utilize the results within a 35° latitudinal and 50° longitudinal distance. The different ratios between the abovementioned outlier and normal groups are attributed not to the co-occurrence of independent stochastic arrivals but to dynamic connections between TCs, as evidenced by enhanced synoptic wave intensity (Fig. 5e,f). Furthermore, we modify the threshold for defining outliers, incrementally increasing from the 0 to the 95th percentile (in 5-percentile intervals) of the Monte Carlo simulations, and calculate the corresponding ratio of subsequent TCs located in the southeastern quadrant to confirm the role of dynamic interactions in increasing TC cluster activity. The sample sizes of the outlier group at each percentile threshold in the climate simulations are sufficiently large to yield robust conclusions (Supplementary Fig. 9). The conclusions remain unchanged when no constraints on distance are applied (Supplementary Fig. 10).

To determine the underlying mechanisms for dynamically connected TC clusters, we composite the differences in SST and synoptic-scale wave intensity according to the deviations of the probabilistic model as follows. In the highresSST-present simulations (1950–2014), we classify the two groups as above the 95th percentile and below 15th percentile. In observations, we divide the years into two groups on the basis of whether the TC cluster frequency reaches the 50th percentile of the probabilistic simulations, to ensure a sufficient and comparable sample size for the two groups, and the results remain consistent when using TC cluster duration for classification (Supplementary Fig. 4). We compute the differences in SST and synoptic-scale wave intensity during the TC season from July to October (JASO) for the WNP[68] and from August to October (ASO) for the NA[69].

Synoptic-scale wave activity

The lower-tropospheric synoptic-scale wave train favours dynamically connected TCs[12,24]. To quantify the synoptic-scale wave activity, we apply a Butterworth bandpass filter to daily zonal and meridional wind data at 850 hPa, with half power at 3 and 7 days (denoted as u^s and v^s, respectively). The standard deviation of the synoptic-scale relative vorticity (ζ^s) is subsequently utilized as a metric for the intensity of the wave train. The synoptic-scale relative vorticity in the spherical coordinate system can be calculated as follows[25,70]:

$$\zeta^s = \frac{\partial v^s}{\partial x} - \frac{\partial u^s}{\partial y} + \frac{u^s}{a}\tan\varphi \quad (1)$$

where ζ^s indicates the synoptic-scale relative vorticity (in s^{-1}), a is the radius of the Earth (in metres) and φ is the latitude (in radians).

To assess the intensity of the synoptic-scale wave train for a specific month, we compute the s.d. of the synoptic-scale relative vorticity in that month in a given grid. This approach allows a detailed analysis of wave train intensity month by month.

HIRAM experiments

To confirm the effects of long-term warming patterns on TC clusters, we conducted numerical experiments using the high-resolution atmospheric general circulation model (HIRAM-C180) developed by the Geophysical Fluid Dynamics Laboratory (detailed in ref. 71). The model features a horizontal resolution of approximately 50 km with 32 vertical levels, making it comparable to the high-resolution climate models used in this study.

We design three experiments, a control (CTRL) run and two future climate (GWLA and GWEL) runs, to elucidate the influence of different warming patterns. The CTRL run is forced by the observed monthly mean SST. The GWLA run is driven by a La Niña-like global warming pattern, represented by the SST in the CTRL run plus the observed SST trend over 1960–2014. In the GWEL run, the model is forced by the SST from the CTRL run combined with an El Niño-like global warming

pattern, derived from the MME of 12 CMIP5 models for the 2006–2099 period under the RCP8.5 scenario (similar to CMIP6-HighResMIP and refs. 72,73). A widely used TC detection algorithm[74] for global climate models is used to detect TCs in the simulations. The model simulations were conducted from January 1990 to December 2009 for each run. In our analysis, differences in TC cluster activity between the GWLA (GWEL) and CTRL runs, evaluated through 55-year resampling repeated 1,000 times, are taken as the response to the La Niña-like (El Niño-like) global warming pattern (Extended Data Fig. 8).

It is important to note that inter-decadal variability in SST may influence the results. To minimize this impact, we selected the period 1960–2014, during which the positive and negative phases of the AMO and Inter-decadal Pacific Oscillation are largely offset[73]. Nevertheless, we found that the La Niña-like global warming pattern persists regardless of the chosen periods (Supplementary Fig. 11), consistent with ref. 41.

Statistical significance test

In our study, all significance tests are conducted at the 95% confidence level. Kendall rank correlation is used to evaluate the correspondence of TC cluster frequency and TC frequency, which measures the similarity of the ordering of the two series when ranked by each of the quantities[75]. Before coupling the probabilistic model with observations and model simulations, we evaluate the independence of TC frequency, duration and genesis time distributions using the chi-squared test. We use the deviations of the probabilistic model from model outputs scaled by the s.d. of residuals in the linear regression model in TC cluster frequency/duration to represent the normalized bias distribution. This approach enables inter-basin comparisons of bias distributions in the probabilistic modelling. To determine the changes in bias distribution between the two periods in the probabilistic model, we conduct a Kolmogorov–Smirnov test. A 1,000-sample bootstrapping approach is applied to evaluate the linear trends in both TC frequency and TC cluster frequency, as well as the differences in TC ratio, SST and synoptic wave intensity between two given periods[76]. The false discovery rate test is also used to assess the significance of grid points in the spatial pattern[77,78]. The uncertainty of the linear regression model is represented by the s.d.

Data availability

The data that support the findings of this study are all openly available online. The best-track TC data with 6-h temporal resolution are available via NCEI at https://www.ncei.noaa.gov/products/international-best-track-archive. The CMIP6-HighResMIP data are openly available via CEDA at https://data.ceda.ac.uk/badc/cmip6/data/CMIP6/HighResMIP. The daily wind fields at pressure levels from MRI-AGCM3-2-H in CMIP6-HighResMIP are available via ESGF at https://aims2.llnl.gov/search/cmip6/. The tropical storm tracks calculated by the TRACK algorithm are available via CEDA at https://catalogue.ceda.ac.uk/uuid/0b42715a7a804290afa9b7e31f5d7753. Hourly reanalysis data on pressure levels from the ERA5 are available via Copernicus at https://cds.climate.copernicus.eu/cdsapp#!/dataset/reanalysis-era5-single-levels?tab=overview and via NCEP/DOE Reanalysis II at https://psl.noaa.gov/data/gridded/data.ncep.reanalysis2.html. ERSST.v5 data from NOAA are available via NOAA at https://psl.noaa.gov/data/gridded/data.noaa.ersst.v5.html. All the map figures (Fig. 5, Extended Data Figs. 6 and 7 and Supplementary Figs. 3, 4, 8 and 11) were generated using Python Cartopy v.0.22.0 (https://doi.org/10.5281/zenodo.1182735) (ref. 79). The data necessary to reproduce the main results are available via Zenodo at https://doi.org/10.5281/zenodo.15383539 (ref. 80).

Code availability

Analysis and figure generation were performed using Python (version 3.9.7). The code and scripts used to calculate the tropical cyclone clusters, perform the probabilistic modelling and generate the figures in the main text are available via Code Ocean at https://doi.org/10.24433/CO.0176970.v2 (ref. 81).

References

49. Knapp, K. R. et al. The International Best Track Archive for Climate Stewardship (IBTrACS): unifying tropical cyclone data. *Bull. Am. Meteorol. Soc.* **91**, 363–376 (2010).
50. Knutson, T. et al. Tropical cyclones and climate change assessment: Part I: detection and attribution. *Bull. Am. Meteorol. Soc.* **100**, 1987–2007 (2019).
51. Huang, B. et al. Extended Reconstructed Sea Surface Temperature, Version 5 (ERSSTv5): upgrades, validations, and intercomparisons. *J. Clim.* **30**, 8179–8205 (2017).
52. Hersbach, H. et al. ERA5 hourly data on pressure levels from 1940 to present. *Copernicus Climate Change Service (C3S) Climate Data Store (CDS)* (2023).
53. Harris, L. M., Lin, S.-J. & Tu, C. High-resolution climate simulations using GFDL HiRAM with a stretched global grid. *J. Clim.* **29**, 4293–4314 (2016).
54. Voldoire, A. et al. Evaluation of CMIP6 DECK experiments with CNRM-CM6-1. *J. Adv. Model. Earth Syst.* **11**, 2177–2213 (2019).
55. Haarsma, R. et al. HighResMIP versions of EC-Earth: EC-Earth3P and EC-Earth3P-HR – description, model computational performance and basic validation. *Geosci. Model Dev.* **13**, 3507–3527 (2020).
56. Roberts, M. J. et al. Description of the resolution hierarchy of the global coupled HadGEM3-GC3.1 model as used in CMIP6 HighResMIP experiments. *Geosci. Model Dev.* **12**, 4999–5028 (2019).
57. Mizuta, R. et al. Extreme precipitation in 150-year continuous simulations by 20-km and 60-km atmospheric general circulation models with dynamical downscaling over Japan by a 20-km regional climate model. *J. Meteorol. Soc. Jpn. Ser. II* **100**, 523–532 (2022).
58. Kodama, C. et al. The Nonhydrostatic ICosahedral Atmospheric Model for CMIP6 HighResMIP simulations (NICAM16-S): experimental design, model description, and impacts of model updates. *Geosci. Model Dev.* **14**, 795–820 (2021).
59. Peng, Y. et al. Tropical cyclogenesis bias over the central North Pacific in CMIP6 simulations. *J. Clim.* **37**, 1231–1248 (2024).
60. Zhao, J. et al. Atmospheric modes fiddling the simulated ENSO impact on tropical cyclone genesis over the Northwest Pacific. *npj Clim. Atmos. Sci.* **6**, 213 (2023).
61. Roberts, M. CMIP6 HighResMIP: tropical storm tracks as calculated by the TRACK algorithm. *Centre for Environmental Data Analysis* (2019).
62. Chen, G. & Huang, R. Interannual variations in mixed Rossby–gravity waves and their impacts on tropical cyclogenesis over the western North Pacific. *J. Clim.* **22**, 535–549 (2009).
63. Song, K. et al. Confidence and uncertainty in simulating tropical cyclone long-term variability using the CMIP6-HighResMIP. *J. Clim.* **35**, 1–42 (2022).
64. Li, Z. & Zhou, W. Poleward migration of tropical cyclones over the western North Pacific in the CMIP6-HighResMIP models constrained by observations. *npj Clim. Atmos. Sci.* **7**, 161 (2024).
65. Hurley, J. V. & Boos, W. R. A global climatology of monsoon low-pressure systems. *Q. J. R. Meteorol. Soc.* **141**, 1049–1064 (2015).
66. Vishnu, S., Boos, W. R. & Collins, W. D. Historical and future trends in South Asian monsoon low pressure systems in a high-resolution model ensemble. *npj Clim. Atmos. Sci.* **6**, 182 (2023).
67. Li, T. & Fu, B. Tropical cyclogenesis associated with Rossby wave energy dispersion of a preexisting typhoon. Part I: satellite data analyses. *J. Atmos. Sci.* **63**, 1377–1389 (2006).

68. Yu, J. et al. Effects of tropical North Atlantic SST on tropical cyclone genesis in the western North Pacific. *Clim. Dyn.* **46**, 865–877 (2016).
69. Sabbatelli, T. A. & Mann, M. E. The influence of climate state variables on Atlantic Tropical Cyclone occurrence rates. *J. Geophys. Res. Atmos.* **112**, D17114 (2007).
70. Li, R. C. Y., Zhou, W. & Li, T. Influences of the Pacific–Japan teleconnection pattern on synoptic-scale variability in the western North Pacific. *J. Clim.* **27**, 140–154 (2014).
71. Zhao, M. et al. Simulations of global hurricane climatology, interannual variability, and response to global warming using a 50-km resolution GCM. *J. Clim.* **22**, 6653–6678 (2009).
72. Zhao, J., Zhan, R. & Wang, Y. Different responses of tropical cyclone tracks over the western North Pacific and North Atlantic to two distinct sea surface temperature warming patterns. *Geophys. Res. Lett.* **47**, e2019GL086923 (2020).
73. Zhao, J. et al. Untangling impacts of global warming and Interdecadal Pacific Oscillation on long-term variability of North Pacific tropical cyclone track density. *Sci. Adv.* **6**, eaba6813 (2020).
74. TSTORMS software code (NOAA, 2025); https://www.gfdl.noaa.gov/tstorms/
75. Kendall, M. G. & Gibbons, J. D. *Rank Correlation Methods* (Oxford Univ. Press, 1990).
76. Mooney, C. Z., Duval, R. D. & Duvall, R. *Bootstrapping: a Nonparametric Approach to Statistical Inference,* Volume 95 (Sage, 1993).
77. Wilks, D. On "field significance" and the false discovery rate. *J. Appl. Meteorol. Climatol.* **45**, 1181–1189 (2006).
78. Wilks, D. "The stippling shows statistically significant grid points": how research results are routinely overstated and overinterpreted, and what to do about it. *Bull. Am. Meteorol. Soc.* **97**, 160309141232001 (2016).
79. Elson, P. et al. SciTools/cartopy: v0.22.0 (Zenodo, 2023).
80. Fu, Z.-H. et al. Data for "Shifting hotspot of tropical cyclone clusters in warming a climate". *Zenodo* https://doi.org/10.5281/zenodo.15383539 (2025).
81. Fu, Z.-H. et al. Shifting hotspot of tropical cyclone clusters in warming a climate. *Code Ocean* https://doi.org/10.24433/CO.0176970.v2 (2025).

Acknowledgements

Z.-H.F., W.Z. and X.W. are jointly supported by the National Natural Science Foundation of China (grants 42288101, 42192563, 424B2026 and 42120104001) and the International Science and Technology Cooperation Program under the 2024 Shanghai Action Plan for Science, Technology and Innovation (24230780200). D.X. and N.L. were supported by the National Oceanic and Atmospheric Administration, US Department of Commerce, under award NA23OAR4320198, at Princeton University. D.X. moved to the University of Hong Kong and was then supported by the start-up fund of HKU 000250348.130087.25300.100.01. The statements, findings, conclusions and recommendations are those of the author(s) and do not necessarily reflect the views of the National Oceanic and Atmospheric Administration or the US Department of Commerce. We thank R. Mizuta for providing the NICAM TC datasets. We thank G. Wang, R. Zhan, R. Zhang and M. Xu for their helpful suggestions.

Author contributions

W.Z. supervised the study. Z.-H.F. and D.X. initiated the idea and designed the research in discussion with S.-P.X., W.Z. and N.L. Z.-H.F. performed the probabilistic modelling, conducted the analysis and produced the figures. J.Z. and J.C.L.C. helped improve the probabilistic model. S.-P.X. and J.Z. suggested further validation in a high-resolution climate model. J.Z. performed the HIRAM experiments. X.W. processed the synoptic-scale wave intensity data. Z.-H.F. and D.X. wrote the initial manuscript. All authors contributed to interpreting the results and improving the manuscript.

Competing interests

The authors declare no competing interests.

Additional information

Extended data is available for this paper at https://doi.org/10.1038/s41558-025-02397-9.

Supplementary information The online version contains supplementary material available at https://doi.org/10.1038/s41558-025-02397-9.

Correspondence and requests for materials should be addressed to Wen Zhou.

Peer review information *Nature Climate Change* thanks Masuo Nakano, Lian Xie and the other, anonymous, reviewer(s) for their contribution to the peer review of this work.

https://doi.org/10.1038/s41558-025-02397-9

Extended Data Table 1 | Quantified contributions (%) of changes in TC statistics to TC cluster changes based on observations

	All	Frequency	Lifespan	Genesis time	Lifespan + Genesis time
	TC cluster frequency				
NA	61.9, [57.2, 67.5]	68.7, [64.1, 74.0]	−1.5, [−5.5, 2.8]	−6.1, [−10.1, −1.5]	−8.5, [−12.3, −4.3]
WNP	87.1, [75.2, 99.4]	70.4, [60.3, 80.9]	10.9, [−0.8, 22.8]	6.8, [−4.3, 18.2]	18.7, [7.6, 29.5]
	TC cluster duration				
NA	99.3, [90.4, 107.9]	128.4, [118.2, 137.6]	−6.2, [−13.6, 0.9]	−11.8, [−19.9, −4.5]	−17.5, [−23.3, −10.4]
WNP	81.6, [72.2, 88.6]	55.8, [48.2, 62.8]	25.4, [19.0, 33.4]	5.8, [−1.9, 12.1]	30.8, [23.0, 38.3]

The contribution is calculated by dividing the TC cluster changes estimated through probabilistic modeling by the observed or modeled changes. Square brackets represent the 5th to 95th percentile of the quantified contributions in the probabilistic simulations.

https://doi.org/10.1038/s41558-025-02397-9

Extended Data Table 2 | Quantified contributions (%) of changes in TC statistics to TC cluster changes based on the MME in seven high-resolution climate models from CMIP6-HighResMIP

	All	Frequency	Lifespan	Genesis time	Lifespan + Genesis time
	TC cluster frequency				
NA	84.5, [73.2, 97.2]	53.4, [38.6, 66.9]	14.1, [1.0, 27.6]	9.7, [−4.9, 22.6]	25.4, [13.2, 38.3]
WNP	54.7, [46.8, 62.2]	46.0, [37.0, 53.9]	5.3, [−3.8, 13.5]	3.7, [−4.7, 11.1]	9.7, [2.6, 16.8]
	TC cluster duration				
NA	111.6, [97.4, 124.9]	50.2, [34.5, 62.7]	29.1, [18.1, 41.5]	14.1, [2.6, 26.0]	47.1, [29.8, 62.3]
WNP	89.7, [80.4, 99.2]	63.2, [53.5, 73.2]	23.4, [14.0, 34.8]	8.4, [−3.3, 20.1]	32.3, [23.2, 43.3]

The contribution is calculated by dividing the TC cluster changes estimated through probabilistic modeling by the observed or modeled changes. Square brackets represent the 5th to 95th percentile of the quantified contributions in the probabilistic simulations.

https://doi.org/10.1038/s41558-025-02397-9

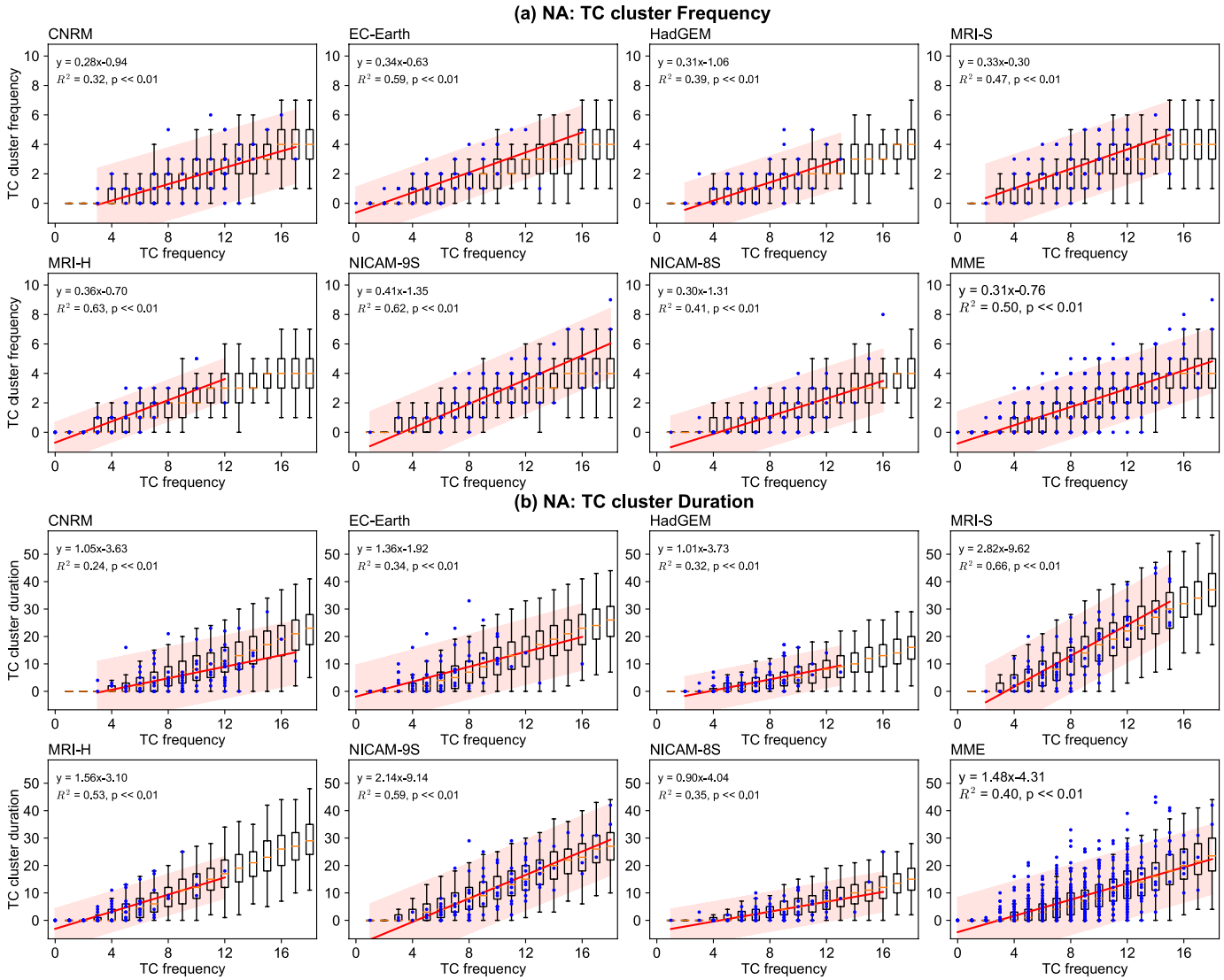

Extended Data Fig. 1 | Performance of the TC cluster probabilistic model in individual models and their MME in the NA. Relationship between yearly TC frequency and yearly TC cluster activity (**a**, frequency; **b**, duration) in model outputs (blue dots) and 1000 Monte Carlo simulations (boxplots) during 1950–2050 in the NA based on seven high-resolution climate models and their MME from CMIP6-HighResMIP. The linear regression models between TC frequency and TC cluster frequency/duration are shown as red lines, with 95% confidence intervals shaded based on the two tailed Student's t-test. The function, R-squared (R^2), and p-value of the models are presented at the upper left. In each boxplot, the box spans from the first quartile to the third quartile of the data, with a line marking the median. The whiskers extend from the box by 1.2× the interquartile range.

https://doi.org/10.1038/s41558-025-02397-9

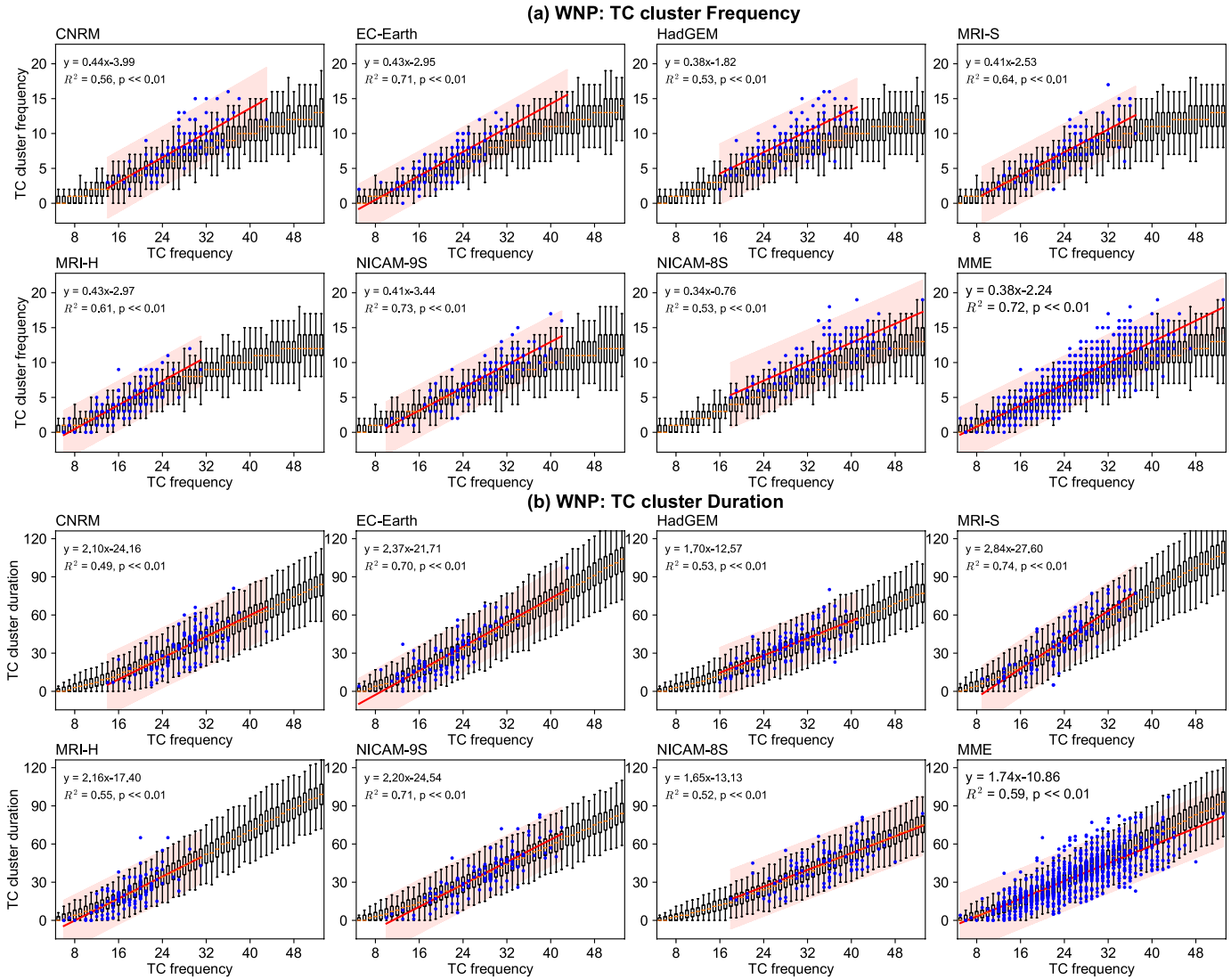

Extended Data Fig. 2 | Performance of the TC cluster probabilistic model in individual models and their MME in the WNP. Relationship between yearly TC frequency and yearly TC cluster activity (**a**, frequency; **b**, duration) in model outputs (blue dots) and 1000 Monte Carlo simulations (boxplots) during 1950–2050 in the WNP based on seven high-resolution climate models and their MME from CMIP6-HighResMIP. The linear regression models between TC frequency and TC cluster frequency/duration are shown as red lines, with 95% confidence intervals shaded based on the two tailed Student's t-test. The function, R-squared (R^2), and p-value of the models are presented at the upper left. In each boxplot, the box spans from the first quartile to the third quartile of the data, with a line marking the median. The whiskers extend from the box by 1.2× the interquartile range.

https://doi.org/10.1038/s41558-025-02397-9

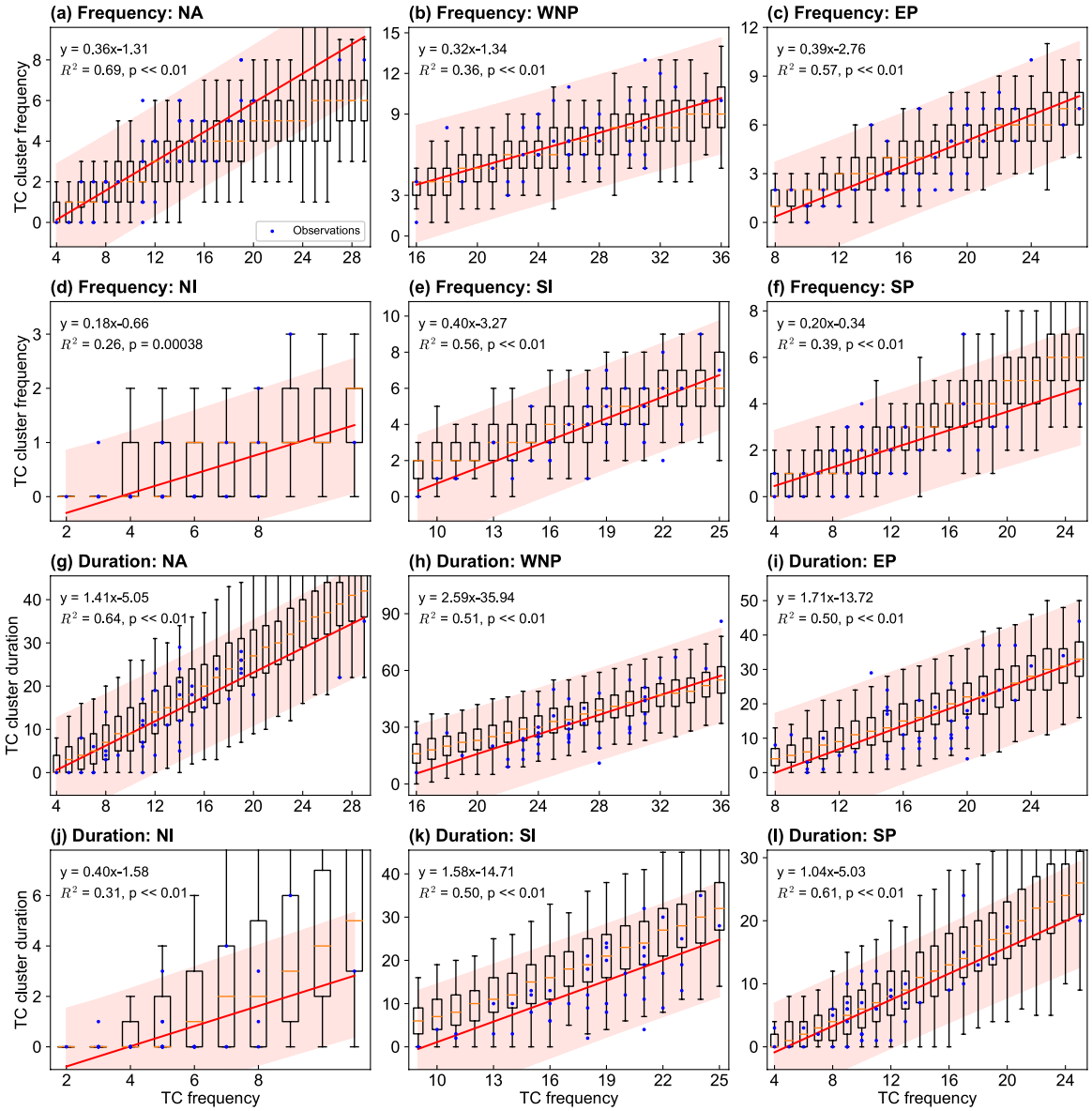

Extended Data Fig. 3 | Performance of the TC cluster probabilistic model in global basins. a–f, Relationship between yearly TC frequency and yearly TC cluster frequency in observations (blue dots) and 1000 Monte Carlo simulations (boxplots) in the six major basins (1979–2024 for the NA and WNP, and 1979–2022 for the other four basins). The linear regression models between TC frequency and TC cluster frequency/duration are shown as red lines, with 95% confidence intervals shaded based on the two tailed Student's t-test. The function, R-squared (R^2), and p-value of the models are presented at the upper left. **g–l**, Same as in **a–f** but for TC cluster duration. In each boxplot, the box spans from the first quartile to the third quartile of the data, with a line marking the median. The whiskers extend from the box by 1.2× the interquartile range. When extending the analysis to the basins in the Southern Hemisphere (that is, South Indian (SI) and South Pacific (SP)), the data are shifted by 182 days (approximately 6 months) to obtain a unimodal distribution of genesis time. Due to the limited sample size and bimodal distribution of TC genesis time in the North Indian (NI) in observations, we divide the TC genesis time based on the median and obtain the corresponding PDF of TC lifespan.

https://doi.org/10.1038/s41558-025-02397-9

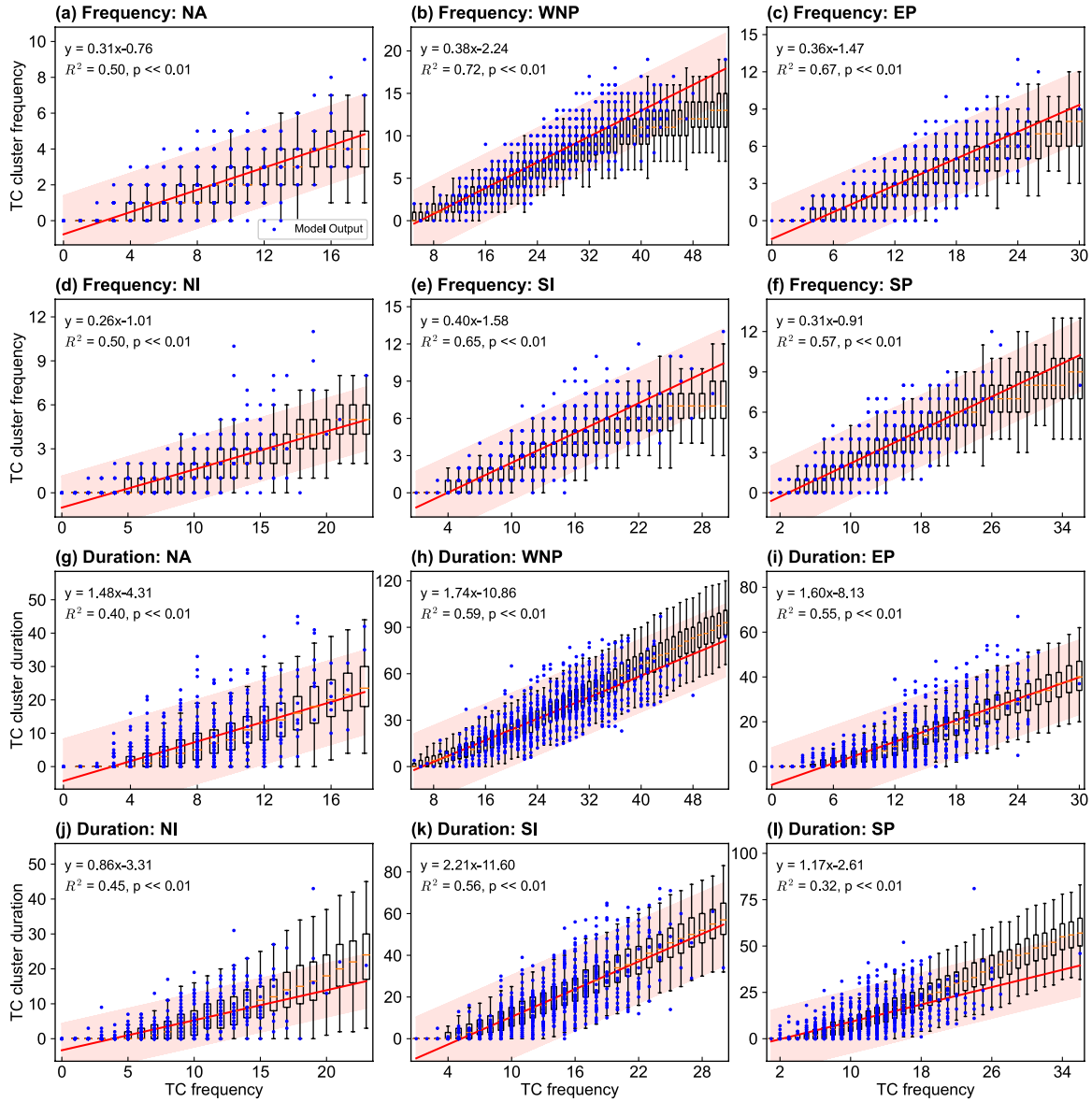

Extended Data Fig. 4 | Performance of the TC cluster probabilistic model in climate models. a–f, Relationship between yearly TC frequency and yearly TC cluster frequency in the model outputs (blue dots) and 1000 Monte Carlo simulations (boxplots) during 1950–2050 in the six major basins based on the MME of seven high-resolution climate models from CMIP6-HighResMIP. The linear regression models between TC frequency and TC cluster frequency/duration are shown as red lines, with 95% confidence intervals shaded based on the two tailed Student's t-test. The function, R-squared (R^2), and p-value of the models are presented at the upper left. **g–l**, Same as in **a–f** but for TC cluster duration. In each boxplot, the box spans from the first quartile to the third quartile of the data, with a line marking the median. The whiskers extend from the box by 1.2× the interquartile range.

https://doi.org/10.1038/s41558-025-02397-9

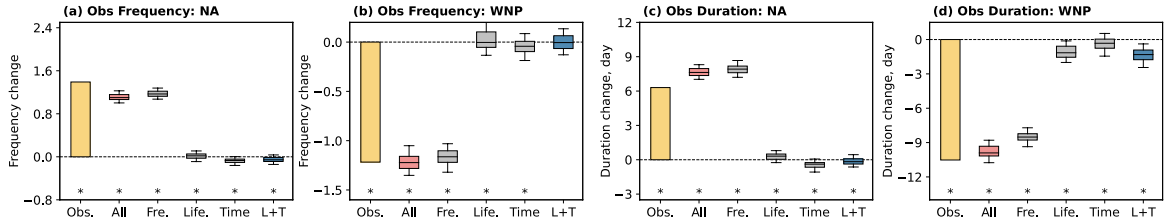

Extended Data Fig. 5 | Quantifying contributions of TC climatology changes to TC cluster changes focusing on long-lived TCs (lasting ≥ 2days). a, **b**, Observed TC cluster frequency change (yellow histogram) and the changes simulated by probabilistic modeling (boxplots) between 1979–2001 and 2002–2024 (the latter minus the former) in the NA (**a**) and WNP (**b**). The contributions from changes in TC climatology ('All') and individual parameters ('Fre.' for TC frequency, 'Life.' for TC lifespan, 'Time.' for TC genesis time, and 'L + T' for the combinations of TC lifespan and genesis time) are simulated by varying the given parameter(s) while keeping the other(s) fixed (Methods). The boxplots show the averages of every 1000 Monte Carlo simulations (in total, 100 averages). The box spans from the first quartile to the third quartile of the data, with a line marking the median. The whiskers represent the range from the 5th to the 95th percentile of the data. Asterisks indicate that the mean value is significantly different from zero at the 95% confidence level based on the 1000-sample bootstrapping. **c**, **d**, Same as in **a**, **b** but for TC cluster duration with periods between 1979–2001 and 2002–2024.

https://doi.org/10.1038/s41558-025-02397-9

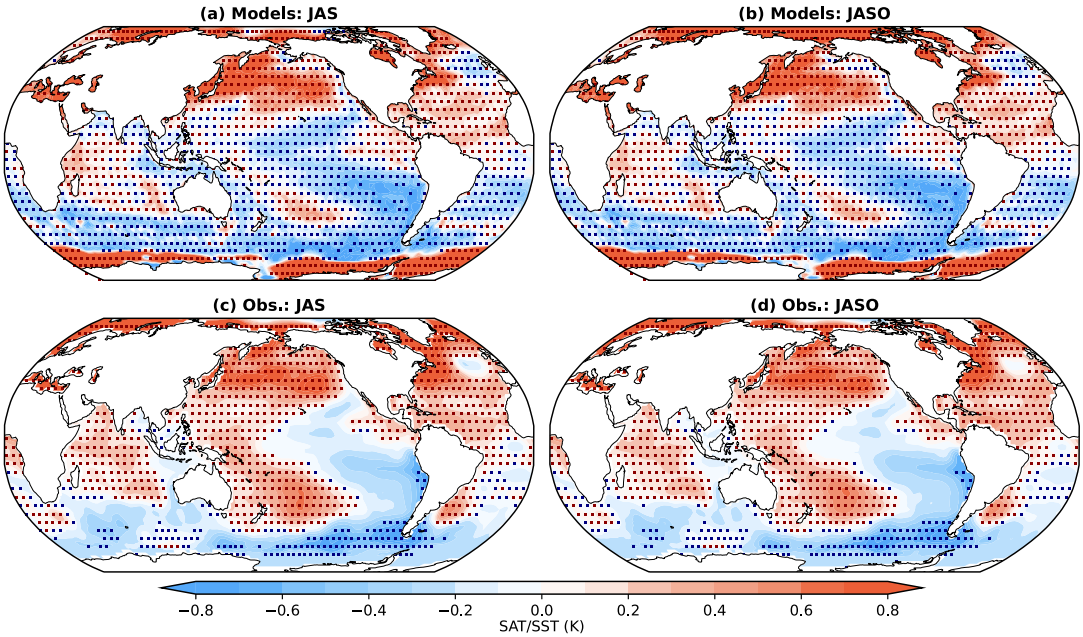

Extended Data Fig. 6 | Patterns of SST changes in observations and climate models. a, **b**, Differences in SAT (K) between 1981–2010 and 2020–2049 based on the MME of the highresSST-present and highresSST-future simulations from CMIP6-HighResMIP. We subtract the tropical mean changes (20°S-20°N) to eliminate the signal of uniform warming. **c**, **d**, Differences in SST (K) between 1979–2001 and 2002–2024 in observations. Averages of changes are shown for TC peak seasons in each basin (that is, JAS for the NA and JASO for the WNP). Dots indicate statistically significant differences at a 95% confidence interval based on the 1000-sample bootstrapping and false discovery rate test. Basemaps from Natural Earth (https://www.naturalearthdata.com).

https://doi.org/10.1038/s41558-025-02397-9

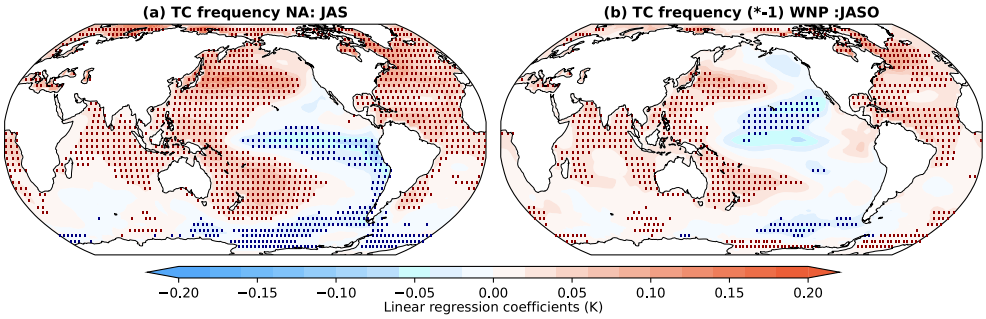

Extended Data Fig. 7 | Patterns of SST that favorable for TC genesis in the NA and WNP. a, **b**, Linear regression coefficients (K) between TC frequency in the NA (**a**) and WNP (**b**; multiplied by −1) with global SST during 1979–2024. The SST are analyzed for TC peak seasons in each basin, indicative of concurrent influences (that is, JAS for the NA and JASO for the WNP). Dots indicate statistically significant differences at a 95% confidence interval based on the 1000-sample bootstrapping and false discovery rate test. The data are not detrended to include the possible influences from recent global warming. Basemaps from Natural Earth (https://www.naturalearthdata.com).

https://doi.org/10.1038/s41558-025-02397-9

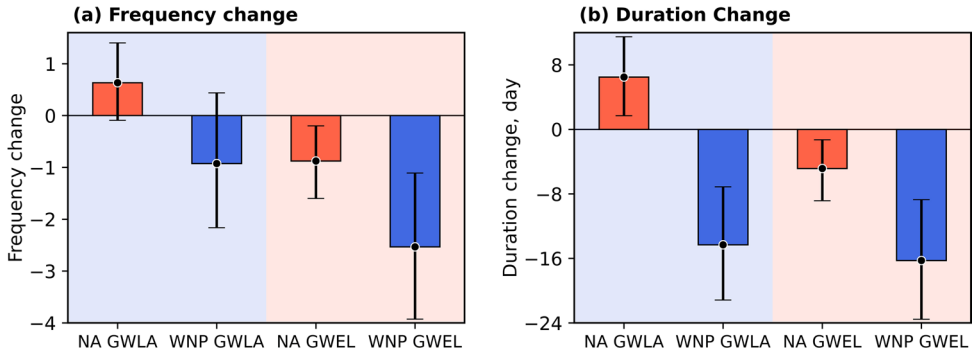

Extended Data Fig. 8 | TC cluster responses to different warming patterns in HIRAM experiments. a, **b**, Differences in TC cluster frequency (**a**) and duration (**b**) over the NA (red bars) and WNP (blue bars) between simulations forced with a La Niña–like global warming pattern (blue shading) and an El Niño–like global warming pattern (red shading) compared to the CTRL simulation. The error bars represent the 95% confidence interval, calculated using 1000-sample bootstrapping. The black dots denote the average value of the differences.